MATERIALS CHEMISTRY FRONTIERS

REVIEW

View Article Online
View Journal | View Issue

Cite this: *Mater. Chem. Front.*, 2024, **8**, 3474

Received 28th December 2023,
Accepted 10th May 2024

DOI: 10.1039/d3qm01340e

rsc.li/frontiers-materials

Solution-processed structural colors and their applications

Wei-Jie Feng, [a] Jennie Paik[a] and L. Jay Guo *[ab]

High-quality and brilliant structural colors have been successfully produced using vacuum-based deposition and patterning technology in recent decades. Nevertheless, the major obstacles of high production costs and limited scalability impede the commercialization of these vibrant color products. Solution-processed structural colors, on the other hand, are renowned for their cost-effectiveness, scalability, and versatility. In this review, we provide an overview of prevalent solution-based techniques for structural color synthesis, along with their potential applications. Emphasizing the versatility of solution-processed structural colors, we discuss their capabilities in both color tuning and new ways of modifying refractive indices of dielectrics.

1. Introduction

The realm of color constitutes a captivating facet of our visual encounters, intriguing both scientists and artists throughout history. The multitude of colors permeating our surroundings arises from the absorption or reflection of light by pigments, dyes, or minerals. This phenomenon is entirely contingent on the inherent optical characteristics of the materials involved. Conversely, an alternative avenue for color generation lies in the properties and arrangement of the structure of, rather than the specific, constituent materials. Visible colors that are produced through the interaction between light and micro- or nano-structures (*e.g.* thin film interference, particle resonance) are commonly referred to as structural colors. Structural colors are prevalent in the natural world,[1,2] where they serve pivotal roles in diverse biological functions such as mate selection, camouflage, and communication. Notable instances include the iridescent hues found in butterfly wings,[3,4] peacock feathers,[5] beetle shells,[6] and bird feathers[7] (Fig. 1). These colors emerge through the interference of light waves with nanostructures inherent in these materials. In contrast to conventional organic dyes, structural colors offer several advantages.[8]

Firstly, they exhibit resistance to fading over time, as their coloration is not produced by chemical substances that could be susceptible to environmental factors like light, heat, or moisture. Secondly, they have the capacity to generate a broader spectrum of colors, deriving their hues from the properties of nanostructures rather than the material composition. Thirdly, and important to this review, their production is feasible using environmentally friendly materials and processes, eliminating dependence on toxic chemicals or heavy metals.

In recent decades, fueled by inspiration drawn from nature, researchers have crafted a myriad of artificial designs for structural

[a] *Macromolecular Science and Engineering, The University of Michigan, Ann Arbor 48109, USA. E-mail: guo@umich.edu*
[b] *Department of Electrical Engineering and Computer Science, The University of Michigan, Ann Arbor 48109, USA*

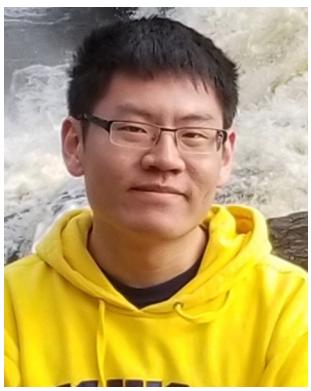

Wei-Jie Feng

Weijie Feng received his PhD degree in Macromolecular Science and Engineering from University of Michigan under the supervision of Prof. L. Jay Guo. His main research interest is in structural color fabrication and nanomaterial synthesis and characterization. He is now employed by Intel Corporation as a defect metrology engineer.

Jennie Paik

Jennie Paik received their B.S. in Chemistry from the University of Massachusetts Amherst in 2018 and is currently a PhD candidate in the Macromolecular Science and Engineering program at the University of Michigan under the supervision of Prof. L. Jay Guo. Their primary research interest is using structure–function relationships in macromolecular networks to develop functional materials.

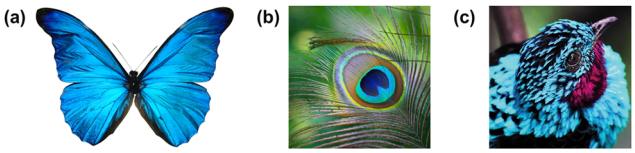

Fig. 1 Examples of structural color in nature. (a) Morpho butterfly with brilliant blue wings, (b) colorful peacock feather, (c) blue feather barb of a male plum-throated coting.

colors. These include photonic crystals,[9–14] metamaterials,[15–17] and plasmonics,[18–23] amongst others, each showcasing a spectrum of color effects characterized by remarkable vibrancy. From the understanding of the inherent physical principles, a multitude of fabrication technologies have emerged to bring these designs to fruition. Techniques such as physical vapor deposition (PVD),[24,25] atomic layer deposition (ALD),[26] sputtering,[27,28] photolithography,[29–32] nanoimprinting,[33,34] self-assembly[35–39] have been developed to realize these intricate designs. Readers can refer to other reviews that cover these technologies and basic principles of colors with respect to human perception.[40] While each method boasts unique strengths and weaknesses, a significant drawback is the reliance on high vacuum conditions[41–44] for film deposition or intricate, multi-step patterning processes[21,32,34,45,46] used by many of these techniques. This limitation significantly hampers their potential applications for large-scale and cost-effective production. In contrast solution-processed deposition methods are immensely desirable for their inherent simplicity, cost-effectiveness, and scalability, thereby rendering large-scale production of structural color coatings significantly more achievable. Moreover, the incorporation of solutions or suspensions introduces substantial versatility in manipulating material composition and morphology. In this comprehensive review, our emphasis will be on the diverse strategies developed to date for solution-based structural color fabrication. We will undertake a thorough comparison of their merits and limitations, accompanied by illustrative examples spanning a wide array of applications. While many photonic structures can indeed be fabricated using traditional vacuum-based processes, we will explore alternative routes through solution processes, where they offer the potential to reduce costs and unlock new possibilities.

The structure of the paper will unfold as follows: Section 2 will present an extensive review of the most widely adopted solution-based methods for structural color fabrication, delving into their underlying chemistry. In Section 3, our focus will shift to one of the most distinctive aspects of solution-processed structural color: tunability. Many examples will be provided to showcase how structural color derived from solutions responds to various external stimuli (such as electricity, temperature, solvent, *etc.*) through spatial tuning, along with their potential applications. We will also explore the feasibility of creating artificial optical materials through refractive index (RI) tuning and elucidate how these novel optical properties contribute to unique color perceptions. Section 4 will offer a comprehensive summary of solution-processed structural color and provide insights into the present challenges as well as future research directions.

2. Solution-based fabrication strategies

2.1. Structural color from self-assembly

2.1.1. Colloidal particle self-assembly. Self-assembly of nanoscale colloidal particles into various photonic structures allows a facile and effective way of generating structural color from the bottom-up. Due to the close packed nature of spherical particles, highly ordered photonic crystals (PhC) derived from inorganic or polymer colloid self-assembly have been widely studied in the past decades. From colloidal particle self-assembly, an opal structure featuring the face-centered-cubic (FCC) packing is observed[47,48] as a result of the most thermodynamic stable state (Fig. 2a), mimicking the color appearance from the natural gemstone, Opal. With well-defined periods, interparticle spacing and material refractive index, photonic bandgaps (PBG) can be generated at specific reflection angle.[49,50] Hence, a structural color can be produced when the PBG is within the visible wavelength range. The center wavelength λ within the PBG can be simply understood with the Bragg model[51] (Fig. 2b): $\lambda = \frac{2nd\cos(\theta_2)}{N}$, where n is the average refractive index, d is the PC period, θ_i is the incident angle, and N is an integer that characterizes the order of the bands.

With a careful tuning of the colloidal particle size and the material composition, self-assembled PCs with various colors can be made. Typical fabrication utilizes a convective assembly method, where the capillary force pushes the mono-dispersed colloidal particle to self-pack into a single-crystal film at the front of an evaporating solution. An early example of silica colloidal particles with sizes from 260–400 nm produces colors in blue, yellow and red (Fig. 3a and b).[52] Other methods, including external field (*i.e.* electric field, gravity, *etc.*) induced PhC self-assembly,[53,54] spin-coating,[55,56] electrospinning,[57] *etc.* were later on developed based on the initial ideal of convective

L. Jay Guo

L. Jay Guo is a Professor of Electrical and Computer Engineering at the University of Michigan. His lab is involved in interdisciplinary research, with activities ranging from polymer-based photonic devices and sensor applications, flexible transparent conductors, structural colors and AI assisted design, hybrid photovoltaics and photodetectors, to nanomanufacturing technologies, and are contributed by students from Electrical Engineering and Optics, Macromolecular Science & Engineering, Applied Physics, Physics, and Mechanical Engineering.

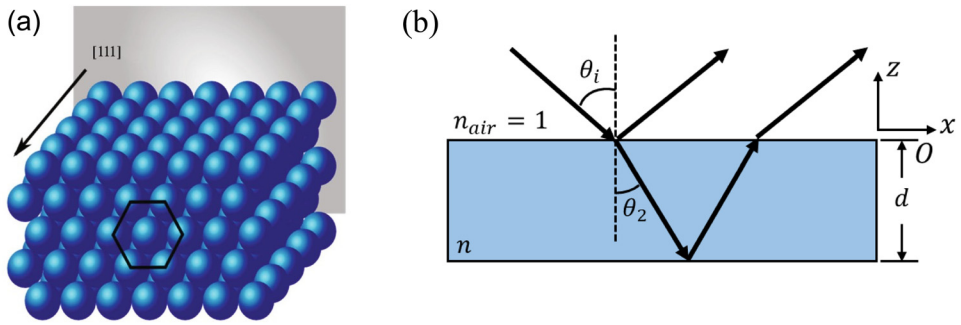

Fig. 2 Schematic illustration of (a) an opal structure [Reproduced from ref. 47, with permission from Springer Publishing, Copyright 2022] and (b) Bragg's law where n is the average refractive index, d is the PC period, θ_i is the incident angle, θ_2 is the angle of refraction (where $\sin\theta_i = n\sin\theta_2$) and N is an integer that characterizes the order of the bands.

assembly, *i.e.* balancing the rate of colloidal particle self-arrangement and the rate of solvent evaporation becomes the key to a highly ordered photonic structure. In addition to the opal structure, much stronger photonic behavior can be realized if a higher dielectric contrast within the system can be obtained, *e.g.* through use of titanium oxide[58] to achieve higher reflectance. By switching to a higher refractive index nanoparticle made of synthetic melanin, Xiao *et al.*[59] has created a self-assembled PhC with a broader stopband. A higher color purity was also obtained with the absorbing nature of melanin where the reflective background is greatly suppressed (Fig. 3c and d). However, the high index PhC structure poses a challenge in the synthesis of high index colloidal particles, namely in size, uniformity, suspension stability, *etc.* Hence, structural modification is employed to enable a universal method of getting high index material into the PhC structure. The opal structure is treated as a template where the air voids in the initial self-assembled opal structure are replaced with a higher refractive index material. The original silica or polymer template is either chemically etched away or thermally decomposed. The resulting inverse opal structure (Fig. 3e) now contains more spherical air void space with higher contrast to backbone material. In an early demonstration with TiO_2 backbone,[60] the PBG widened and gave a stronger iridescent color appearance. Other metal oxide[61–63] (*e.g.* SnO_2, ZrO_2, *etc.*) were also demonstrated to give vivid color across the entire visible spectrum.

While highly ordered close-packed colloidal particles gives crystalline structure (Fig. 4a), it makes the stopband center

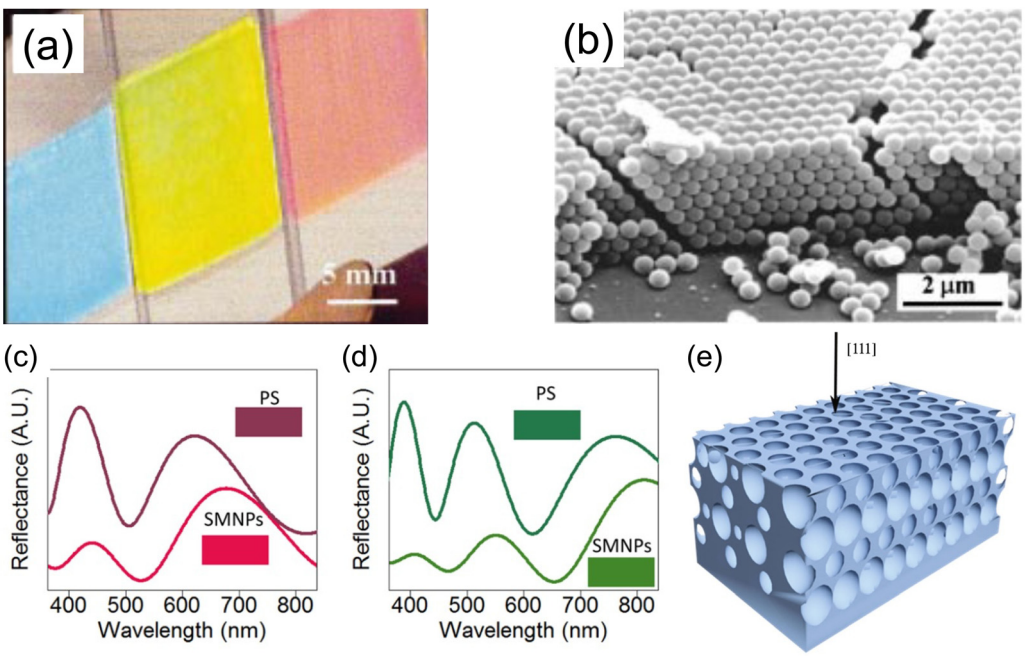

Fig. 3 (a) Structural color of SiO_2 colloidal particle self-assembled photonic crystal. (b) SEM of photonic crystal showing the arrangement of SiO_2 particles. [Reproduced from ref. 52, with permission from American Chemical Society, Copyright 1999]. (c) and (d) Reflection spectra showing the suppression of background reflection with light absorbing synthetic melanin nanoparticles (SMNP). [Reproduced from ref. 59, with permission from American Chemical Society, Copyright 2015]. (e) Schematic illustration of an inverse-opal structure. [Reproduced from ref. 60, with permission from American Association for the Advancement of Science, Copyright 1998].

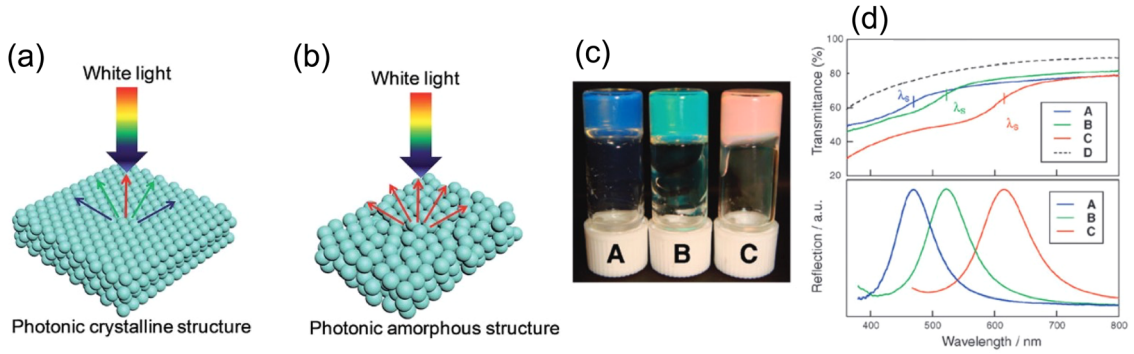

Fig. 4 Schematic illustration of (a) photonic crystal (PhC) and (b) photonic glass (PhG) showing specular and diffusive reflection. [Reproduced from ref. 64, with permission from Royal Society of Chemistry, Copyright 2019]. (c) Glassy colloidal arrays in liquid crystal showing structural color and (d) their corresponding reflection spectra. [Reproduced from ref. 65, with permission from American Chemical Society, Copyright 2009; Reproduced from ref. 66, with permission from Royal Society of Chemistry, Copyright 2009].

wavelength angle dependent as light shines upon different crystal planes producing varied optical phases; thus, iridescent color is always present. Though appealing, consistent color perception is desired in many applications, which cannot be satisfied by the self-assembly accompanied by the long-range order. Besides, the spontaneous nature of self-assembly cannot ensure a perfect crystalline structure throughout the macroscopic film, tiny assembly defects could deteriorate the local color appearance and challenge the large-scale color uniformity. Hence, another colloidal self-assembly structure featuring short range order but long-range disorder[64] (Fig. 4b), in the form of amorphous photonic crystal or photonic glass (PhG), opens another path for non-iridescent structural color generation. With the lack of long-range ordering, PhG-based structural color appears to be more diffusive and non-iridescent. In contrast to balancing the solvent evaporation rate and colloidal self-assembly rate, locking/disturbing/freezing the assembly process of colloidal particles ensures a long-range disorder in PhG. One commonly used method utilizes a glass phase transition of the colloidal system. As shown in Fig. 4c and d, a polymeric gel particle underwent a phase transition, forming a non-closed-packed state as the gel suspension concentration increased. Distinctive color from blue to green to red can be produced[65,66] with various average inter-particle distances from differences in particle surface coverage. Another fabrication method adopts the nature of spinodal phase separation. This strategy has been widely adopted by nature where bird feather barbs show a spinodal deposition phase of the keratin structure, leading to a brilliant blue color.[7,67,68] A template-based synthesis using the feather barb with sol–gel chemistry leads to an inorganic replica of similar structural color[69,70] (Fig. 5a–c). To the best of our knowledge, no direct bottom-up self-assembled PhG structural color has been made with spinodal decomposition. However, a dewetting process during thermal anneal can produce a similar pattern but in 2D. With the dewetted pattern as a litho-free mask, followed by a metal-assisted chemical etch process, a colored silicon substrate can be made[71] (Fig. 5d and e). Other methods including spray coating[72] or rapid thermal evaporation also work well by having these colloidal particles lose their mobility before entering the thermodynamic equilibrium state.

In addition to PhC and PhG, a transition in the assembly ordering can be realized with the co-assembly of colloidal particles of various size.[74,75] By varying the fill fraction of the bi-disperse particles (one small and one large in size),[73] the assembly structure gradually changes from a highly ordered PhC to disordered PhG (Fig. 5f), thus changing from specular color appearance to a more diffusive one. The reflection peak wavelength is therefore a superposition of the diffraction wavelengths for crystalline structures composed of only small or large particles.

2.1.2. Non-spherical colloidal particle self-assembly. In addition to spherical colloidal particles, non-spherical particles can self-assemble to produce color. Initial attempts have been made by stretching self-assembled poly(vinyl alcohol) (PVA) PhC below the glass transition temperature[76](Fig. 6a). An ellipsoidal particle shape is obtained upon cooling and the color is preserved. Though challenging, direct self-assembly of ellipsoidal particles is accessible with the application of external field. Ellipsoidal γ-Fe_2O_3–SiO_2 core–shell particles were synthesized with different aspect ratios and self-assembled under a magnetic field[54] (Fig. 6b). The external magnetic field facilitates the alignment of the ellipsoidal particles, while the positional order could be determined by the particles themselves. The incorporation of the SiO_2 shell modifies the aspect ratio of the original γ-Fe_2O_3 particle and results in various structural colors. Other than ellipsoids, discoidal particles could also be synthesized and self-assembled into PhCs or PhGs. Liu *et al.*[77] carried out a detailed study on structure-color response relation with discoidal polystyrene (PS) particles (Fig. 6c). The PS particles were fabricated with a uniaxial heat compression method in a PVA matrix, where the PS spheres deformed into a discoidal shape. The deformed particles with various aspect ratios then underwent a convective assembly process forming a series of colored films. Both experimental investigation and Monte Carlo/FDTD simulation suggest that larger anisotropy increases the disordering of the assembled structure, leading to a more PhG-like behavior.

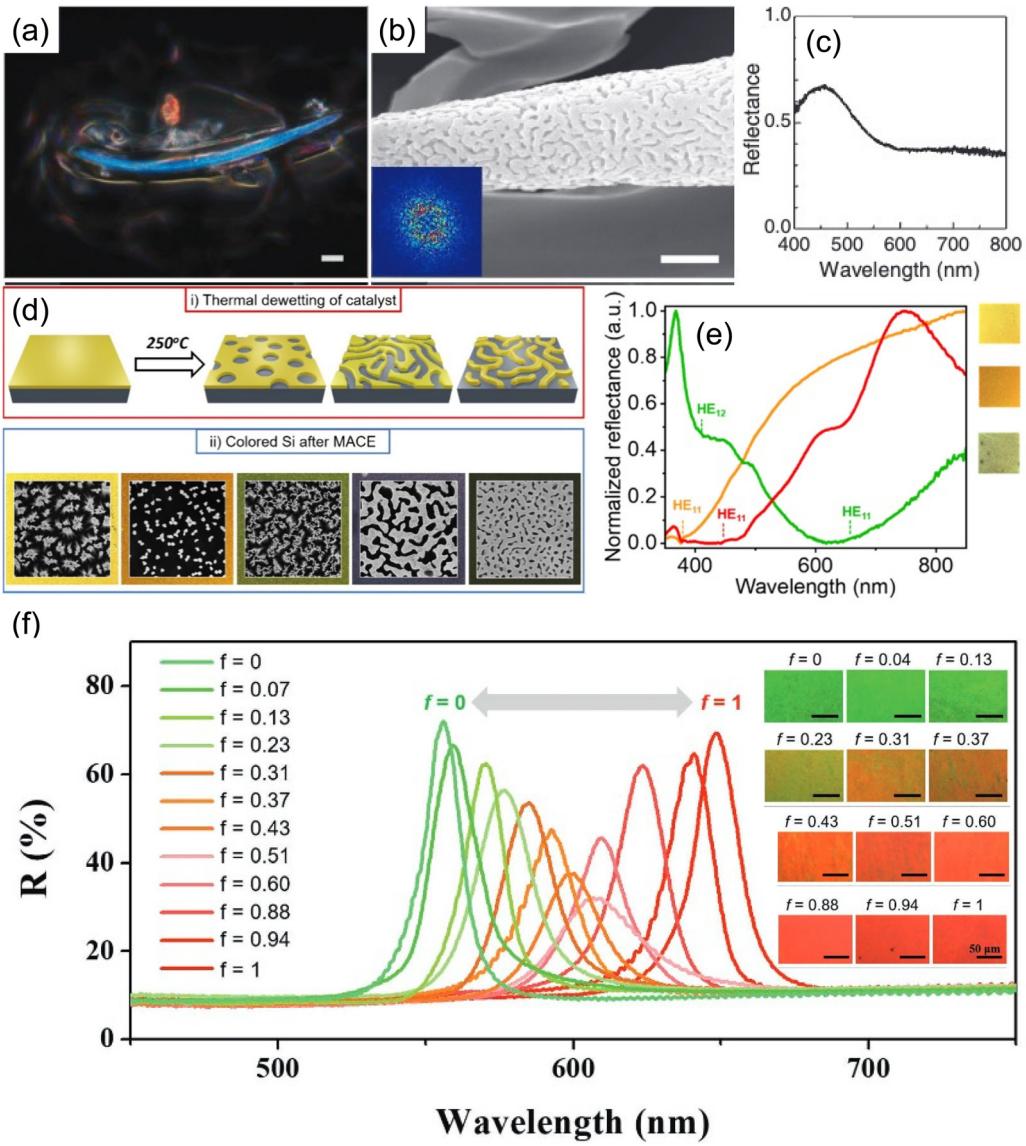

Fig. 5 (a) Spinodal phase of SiO_2 structural color using beetle elytral surface as template and its (b) SEM image and (c) reflection spectrum. [Reproduced from ref. 66,70, with permission from Royal Society of Chemistry, Copyright 2009 and 2013]. (d) Schematic illustration of thermal dewetting followed by metal-assisted chemical etching (MACE) for color Si fabrication. (e) Optical images and reflection spectra of color Si. [Reproduced from ref. 71, with permission from American Chemical Society, Copyright 2023]. (f) Color transition from green to red by changing the ratio of two nanocolloids with different sizes. The reflection spectra showing the transition from specular reflection to diffusive reflection. [Reproduced from ref. 73, with permission from American Chemical Society, Copyright 2019].

While the assembly of high-aspect ratio particles either leads to a disordered structure or nematic-like liquid crystal phase (not capable of forming a well-defined stopband), a slight twist at the particle level makes a different story. Many plants and fruits[78,79] take advantage of the twist in their cell walls (Fig. 7a), where cellulose fiber aligns and twists into a chiral nematic phase (Fig. 7b), leaving a well-defined pitch in between. These helical structures serve as chiral Bragg-reflectors, creating stopbands for light with certain circular polarization. This leads to stunning structural colors. This masterpiece has been replicated by artificially synthesizing a high aspect ratio (~15–20) cellulose nanocrystal (CNC). CNCs can be derived directly from paper pulp through sulfuric acid hydrolysis, where the amorphous region of the cellulose fibers is decomposed while the crystalline region is preserved.[80] Fig. 7c gives an overview of the self-assembly process of CNC.[81–89] A typical CNC could have a rod-like shape with a diameter of 10–20 nm and length of 150–200 nm. The chiral natural of the glucose unit within the cellulose backbone gives a twist to the CNC surface and enables the self-assembly into the chiral nematic phase. The stopband wavelength is determined by the pitch within the assembled helix, where the resonance wavelength λ is a function of pitch length p, the film refractive index n and the angle of incidence θ according to the de Vries formula[90] $\lambda = np\cos(\theta)$. The chiral nature of the film also imposes selectivity in light polarization upon reflection, giving around 50% reflection within the photonic stopband

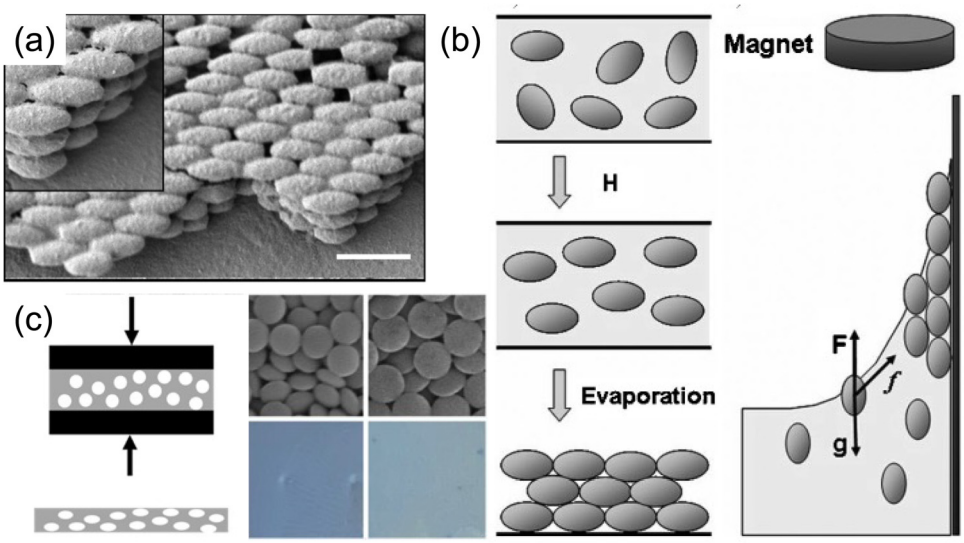

Fig. 6 (a) SEM image of stretched PVA photonic crystal. [Reproduced from ref. 76, with permission from American Chemical Society, Copyright 2009]. (b) Schematic illustration of magnetic field induced γ-Fe_2O_3–SiO_2 particles elongation. [Reproduced from ref. 54, with permission from Wiley-VCH Verlag GmbH & Co. KGaA, Weinheim, Copyright 2009]. (c) Synthesis of heat compressed discoidal particles and their self-assembled structural color. [Reproduced from ref. 77, with permission from American Chemical Society, Copyright 2022].

(Fig. 8a). With the addition of small molecular additives,[87,91–96] a spectrum of the colors from violet to red can be produced continuously by varying the CNC-additive ratio (Fig. 8b, *e.g.* adding L-arginine). Continuous roll-to-roll fabrication of the

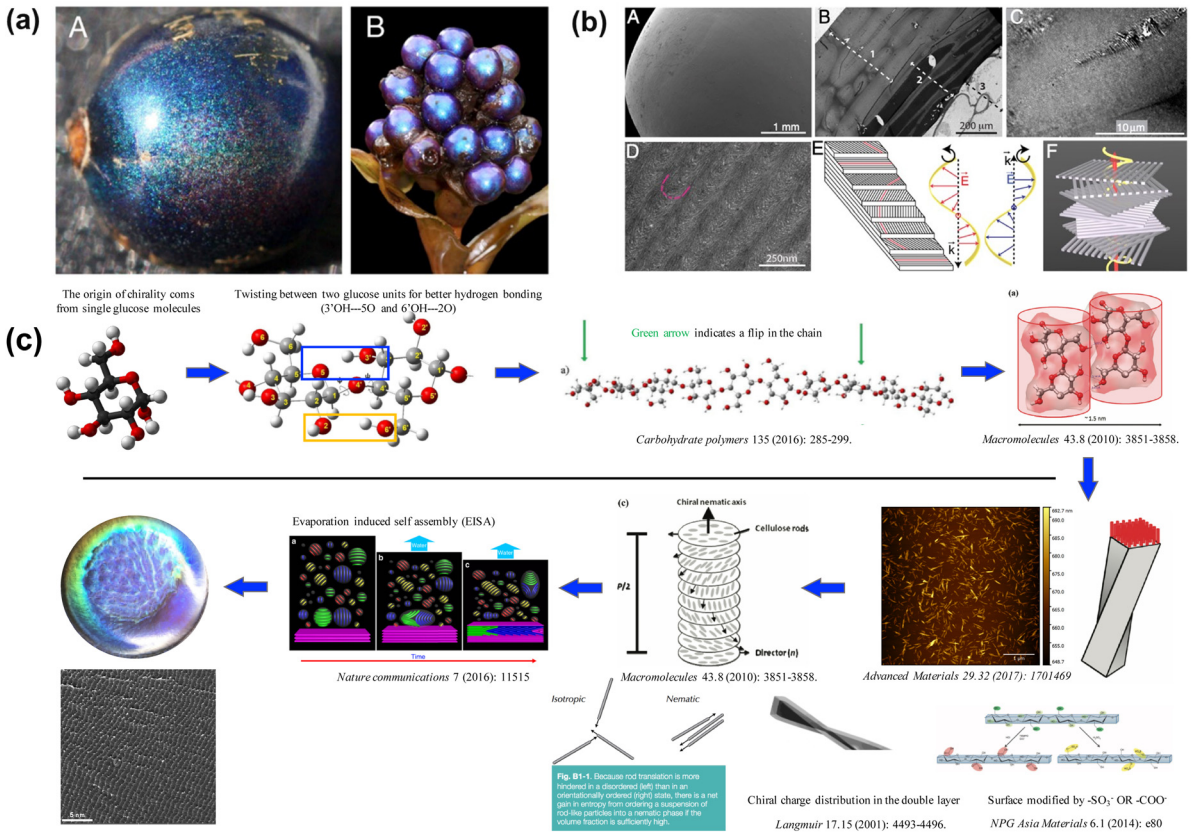

Fig. 7 (a) Photo of *Pollia condensate pericarp*. (b) Microscope image of the helicoidal cell walls. [Reproduced from ref. 78, with permission from National Academy of Science, Copyright 2012; Reproduced from ref. 79, with permission from Wiley-VCH Verlag GmbH & Co. KGaA, Weinheim, Copyright 2013]. (c) Schematic illustration of evaporation-induced self-assembly of CNC. The chiral nature of glucose is passed all the way up to the super-molecular structure.

CNC film under controlled solvent evaporation give brilliant structural color pigments for future scalable production.[97]

2.1.3. Polymer self-assembly. Macromolecules with size much smaller than colloidal particles are also capable of self-assembly into structural colors. Similar to CNC, hydroxypropyl cellulose (HPC), a rigid polysaccharide polymer with a typical persistence length of 6–12 nm,[98] is capable of self-assemble into a mechanochromic chiral nematic phase above the critical concentration.[90,99–103] A gel-like liquid crystal with brilliant structural color can be easily obtained by simply mixing HPC powder with water. However, maintaining the water content inside the HPC liquid crystal is critical for to preserve the color, where a loss of water will lead to a blue shift of color due to reduced pitch. As the film dries, eventually only UV is reflected and visible color is no longer observed. Therefore, good encapsulation of the HPC liquid crystal with water-impermeable polymer substrate, such as polyethylene terephthalate (PET), is necessary for large-scale production.[104] On the other hand, the lyotropic property also enables a facile method of tuning the liquid crystal pitch by varying the HPC concentration, leading to various colors from red to purple across the visible spectrum (Fig. 8c). The color can also be affected by the lower critical solution temperature (LCST) property of HPC, where it undergoes a phase transition as the HPC gets heated.[98,105] The phase segregation of between HPC polymer and water leads to strong scattering of the light, switching the structural-colored gel into white.

Most polymer self-assembly falls in the category of block copolymers (BCPs), where the polymer backbone is made of two or more units with distinctive chemical properties. Phase separation between these distinctive backbone segments enables various ordered structures from lamellae, to cylinders, to close-packed micelles[106] (Fig. 9a and b) and more depending on the relative ratio of the segments. Though the assembly morphology as well as the BCP formulation has been widely investigated, it's quite challenging for these BCP assembled domains to reach the size capable of producing structural colors. The major difficulty lies in synthesizing sufficiently large molecular weight polymers as well as achieving large refractive index contrast between the domains. A commonly used strategy to bring structural color to BCP assembly is by expanding the domain size with external stimuli, which at the same time modulates the refractive index of the domain. Hence, functional chemical groups responsive to external stimuli are frequently incorporated into the BCP backbone. One popular candidate is 2-vinyl pyridine, where a reversible quaternization can be made with various stimuli. In an early attempt, the polystyrene-*block*-poly(2-vinyl pyridine) (PS-*b*-P2VP) self-assembly lamellae, the P2VP domain was swelled (and the domain refractive index was lowered) in reduced salt concentrations to give a photonic stopband near the infrared (Fig. 9c).[107] Further modulation of the PS-P2VP system also involved stimuli as pH,[108] solvents,[109,110] and temperature,[111] among others. Other BCP assembly phases including gyroid[112,113] and micelles[114] are also made possible with delicate polymer design and concentration control. Following the idea of template synthesis, a degradable BCP template was used to achieve large index contrast between the distinctive domains. With the exposure to UV light, the PMMA domain undergoes photo-degradation, which can be removed in acetic acid in a

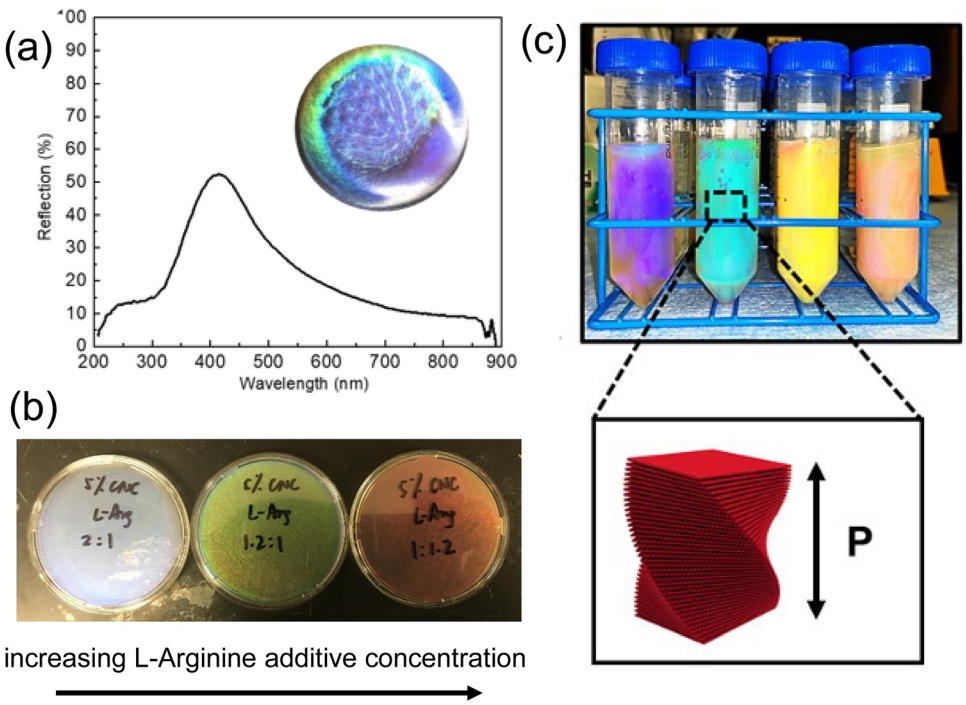

Fig. 8 (a) Reflection spectra of self-assembled CNC film illuminated under unpolarized light. (b) Photo of CNC/L-arginine co-assembled film showing blue, green, and red color with increasing arginine concentration. (c) Photo of HPC liquid crystal with various concentrations.

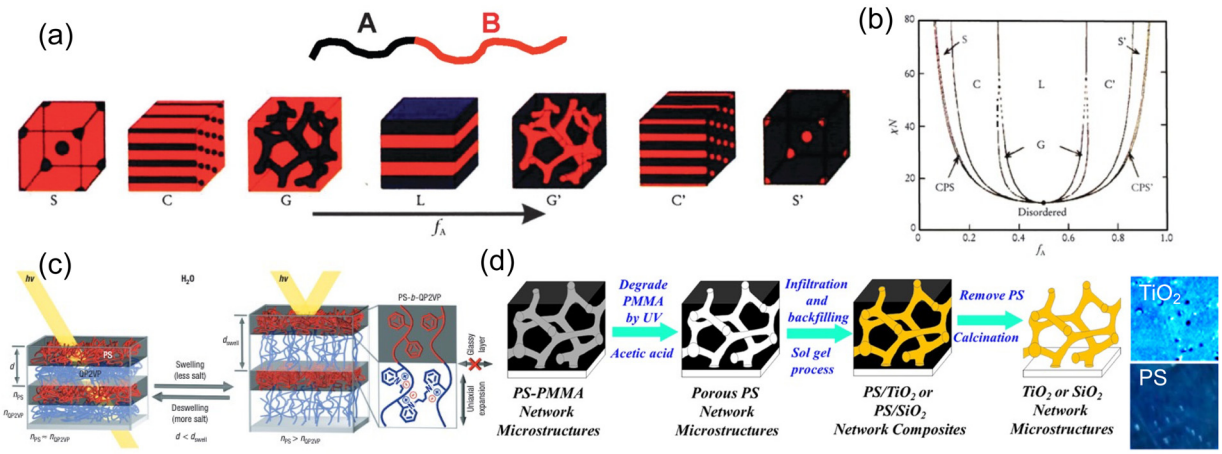

Fig. 9 (a) Various self-assembly phases of BCP and (b) phase diagram. [Reproduced from ref. 106, with permission from Royal Society of Chemistry, Copyright 2012]. (c) Photo-responsive PS-P2VP BCP showing reversible color changes. [Reproduced from ref. 107, with permission from Nature Publishing Group, Copyright 2007]. (d) TiO_2 gyroid structural color made out of BCP self-assembly template. [Reproduced from ref. 113, with permission from American Chemical Society, Copyright 2018].

polystyrene-*block*-poly(methyl methacrylate) (PS-*b*-PMMA) assembled gyroid structure.[113] A replacement is then made with the infiltration of high refractive index oxide (*e.g.* TiO_2) precursor under sol–gel process to give a more brilliant blue color (Fig. 9d).

An alternative strategy for fabricating larger BCP self-assembly domains is *via* brush block copolymers (BBCPs) where various distinctive polymer side chains are grafted to a linear polymer backbone. The increasing degree of polymerization (DP) as well as the longer side chain significantly expand the self-assembly domain size, and no external stimuli is needed to further push the domain scale into visible wavelength. Grafting through ring opening metathesis polymerization (ROMP) is a common strategy for BBCP synthesis[115] (Fig. 10a). A widely studied ω-norbornenyl based backbone is typically adopted due to its easy accessibility and structural rigidity. Macromonomer (MM) moieties like polystyrene, polyhydroxystyrene,[116] poly(methyl methacrylate)[117,118] *etc.* are frequently used as sides chains to enable BBCP structural colors. Yu *et al.* developed a graft through method of BBCP synthesis of ω-norbornenyl polystyrene (NPSt) and ω-norbornenyl poly(4-*tert*-butoxystyrene) (NPtBOS) *via* ROMP.[119] Over 10 BBCPs with various molecular weights (MWs) have been synthesized with lamellae domain sizes ranging from 40 nm to 200 nm. These self-assembled structures are much larger compared to a high-DP linear BCP and can produce structural coloration from blue to pink (Fig. 10b). Note that the alkyl spacer unit in the MMs are the key to enable a high MW synthesis, where the bulky side chain steric hinderance is being mitigated. However, these flexible alkyl chains could reduce backbone rigidity and lead to an insufficient increase in domain sizing.[118] One method of bypassing the incorporation of the flexible spacer while maintaining a sufficient domain size is by introducing a semicrystalline BBCP with poly(ethylene oxide) (PEO). A hierarchical structure of both lamellae and crystalized PEO domains (Fig. 10c) is formed under annealing.[120] In addition, a large refractive index change from 1.46 to 1.64 has been observed upon PEO domain crystallization hence giving a more brilliant color appearance. Shape-memory characteristics are also observed due to well-defined PEO phase transition temperature. Another strategy to compromise the steric hinderance-backbone rigidity dilemma is a dendritic design of MM side chain with BBCP. An AB_3-type MM with dodecyl and fluorobenzyl units radiates from the center benzyl ring into three branches,[121] forming a wedge-like shape with increased steric hinderance but less flexibility. Thus, these wedge-like units give enough MM accessibility during ROMP for high MW BBCP synthesis while keeping the backbone rigidity. The bulk BBCP is then extruded into filament for 3D printing into various geometrically different structural colored objects (Fig. 10d). A spin-off company named "Cypris" is now demonstrating even more promising BBCP-based structural color paints (Fig. 10e) for industrial scale production.[122] Astonishing rainbow color from blue to red shows up only after several minutes of paint drying.

In summary, the self-assembly of nanocolloids and polymers presents a straightforward approach to producing large-scale structural color. This process relies on the intermolecular forces between particles and thus can be easily scale up for bulk production. In addition, minimal external energy is usually required for the assembly process compared to traditional vacuum-based deposition methods. As a result, significant energy savings are achieved. However, structural defects from the self-assembly process poses a big challenge in the way of commercializing self-assembled structural color, where large scale color uniformity can hardly be guaranteed. Therefore, grinding self-assembled structural color into micro-pigments provides a potential method for its real-world application.

2.2. Multilayer coating

As demonstrated in the previous section, photonic crystals synthesized through nanoparticles or block-copolymer self-assembly gives various colors; however, their color properties are largely compromised when ground into micro/nano-flakes for general coating applications. Moreover, these photonic crystals usually take several to hundreds of micron thicknesses

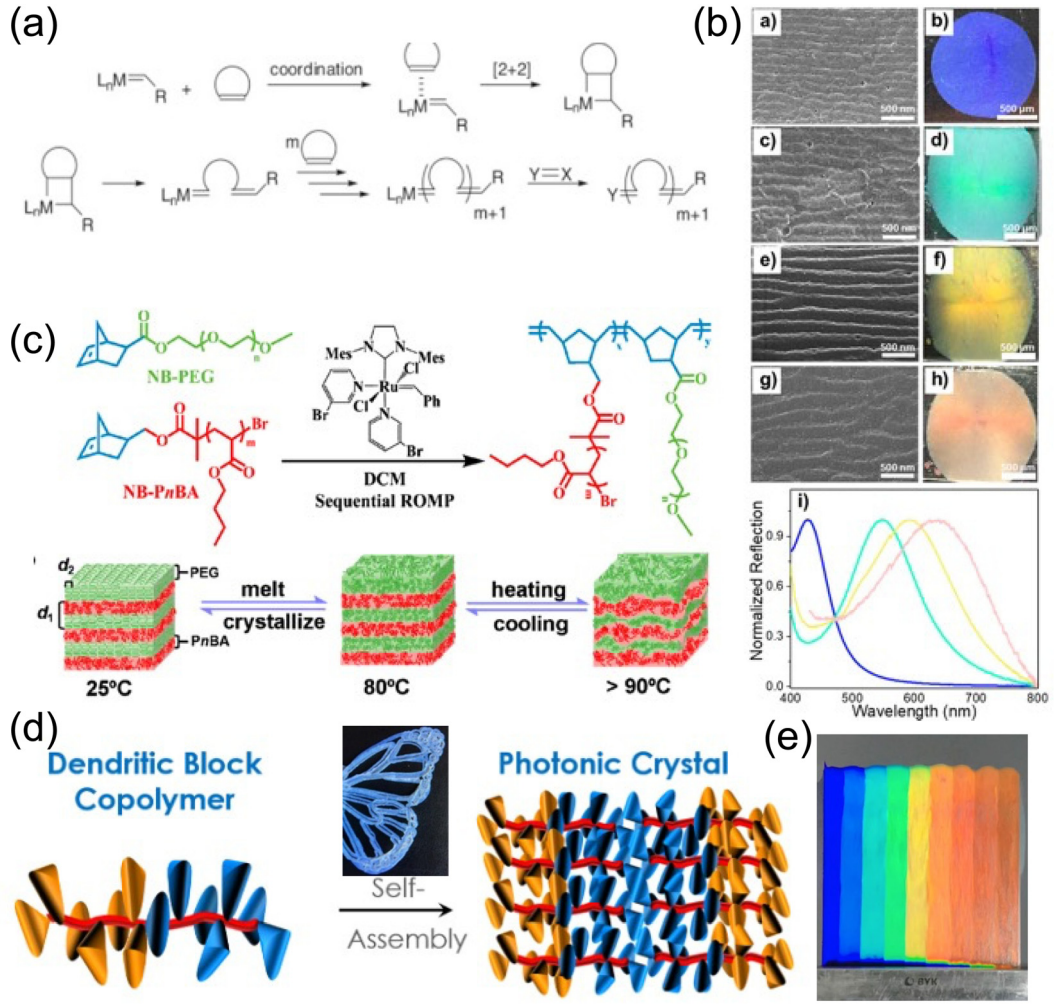

Fig. 10 (a) Illustration of ring opening metathesis polymerization (ROMP) process. [Reproduced from ref. 115, with permission from Elsevier Publishing Group, Copyright 2007]. (b) Self-assembly of BBCP with NPSt and NPtBOS. [Reproduced from ref. 118, with permission from American Chemical Society, Copyright 2019]. (c) A hierarchical lamellar BBCP with crystalizing PEO for structural memory photonic crystal. [Reproduced from ref. 120, with permission from American Chemical Society, Copyright 2020]. (d) Synthetic strategy of AB_3-type BBCP for 3D structural color printing. [Reproduced from ref. 121, with permission from American Chemical Society, Copyright 2017]. (e) Rainbow structural color produced by Cypris Materials Inc. [Reproduced from ref. 122, with permission from Cypris Materials Inc, Copyright 2023].

(*i.e.* CNC or HPC films) to achieve high color brilliance, which largely limits their application in thin film coatings. Multilayer pearlescent pigments, on the other hand, utilize light interference to give brilliant color with sub-micrometer film thickness. Typical thin-film coating methods (Fig. 11)[123] from solution phase includes dip-coating,[124,125] spin-coating,[126] and spray coating.

2.2.1. Layer-by-layer assembly (LbL) coated structural color pigments. Layer-by-layer (LbL) coating utilizes the electrostatic attraction of polyelectrolytes of opposite charges, leading to sequential absorption of layers of alternating positive and negative charges forming a multilayer stack. Hence, LbL coating[127,128] provides a solid platform for creating conformal multilayer structural colors, regardless of the curvature of the substrate. As shown in Fig. 12a, A pre-cleaned or functionalized substrate (*e.g.* glass) is dipped into a solution with highly charged polyelectrolyte such as poly(allyamine hydrochloride) (PAH, positively charged), poly(vinyl sulfate) (PVS, negatively charged), poly(sodium 4-styrenesulfonate) (SPS, negatively charged), or poly(diallyldimethyl ammonium chloride) (PDAC, positively charged). The substrate is rinsed multiple times to remove loosely absorbed molecules then dipped into a polyelectrolyte solution with the opposite charge. The dipping process is then performed in multiple cycles until a desired number of layers are coated on the surface.

To create a reflection stopband centered at λ_0, a quarter-wave Bragg stack with alternating high index (n_H) and low index (n_L) satisfying $n_H d_H = n_L d_L = \lambda_0$ is anticipated, where d_H and = d_L represent the thicknesses of the high index and low index layers respectively. Inorganic nanoparticles like SiO_2 and TiO_2 are commonly introduced to increase the layer index contrast,[129] as demonstrated in Fig. 12b. A bilayer structure with a cation–anion pair (*e.g.* PAH-SiO_2 or TiO_2-PVS) is first formed by two-step LbL coating, featuring a thickness of a few nanometers (mainly determined by the size of nanoparticles). The resulting bilayer coating process is then repeated multiple times to

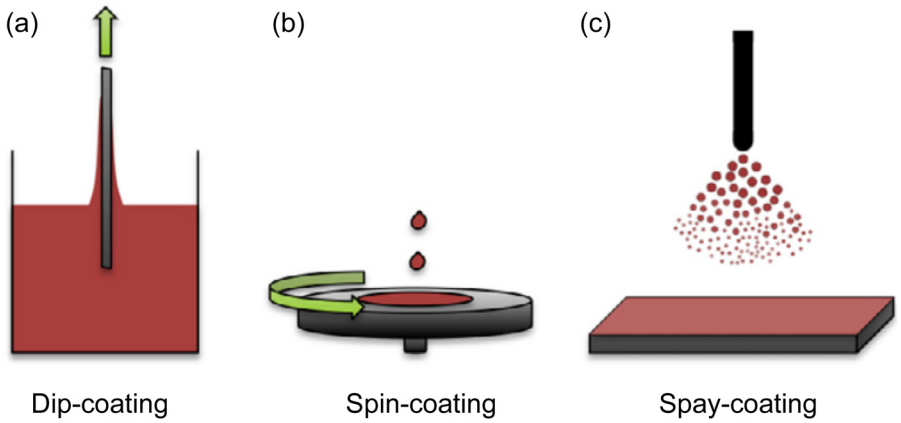

Fig. 11 Schematic illustration of three commonly used thin film coating method (a) dip-coating, (b) spin-coating and (c) spray coating. [Reproduced from ref. 123, with permission from Taylor and Francis Publishing Group, Copyright 2013].

achieve desired thickness. With proper tuning of the LbL cycles and further calcination (to remove the organic component), a SiO_2/TiO_2 Bragg stack is formed with a stopband centered in a visible wavelength. As the removal of the polyelectrolyte leads to a collapse of the nanoparticle assembly, the index of the layer could be fine-tuned according to the particle size and the choice of the polyelectrolyte, allowing customization of the stack properties. Though the charged polyelectrolyte typically results in a hydrophilic coated surface, the rich solution chemistry enables hydrophobic polymer incorporation into the polyelectrolyte framework and thus expands the potential of LbL coating. In a recent example, Yu *et al.*[130] fabricated a hydrophobic structural color coating by introducing hydrophobic PMMA particles (prepared with negative charge) into PDAC layer (Fig. 12c). The as prepared structural colored TiO_2/PMMA stack thus becomes capable of changing its color appearance upon organic vapor uptake.

Compared to dip-coating LbL, which takes a very long time to complete the entire stack considering the thickness of a single bi-layer coating, spray coating provides a more efficient strategy for LbL stack fabrication. As shown in Fig. 12d,[131] a spray-coated TiO_2/SiO_2 LbL film was fabricated *via* multiple

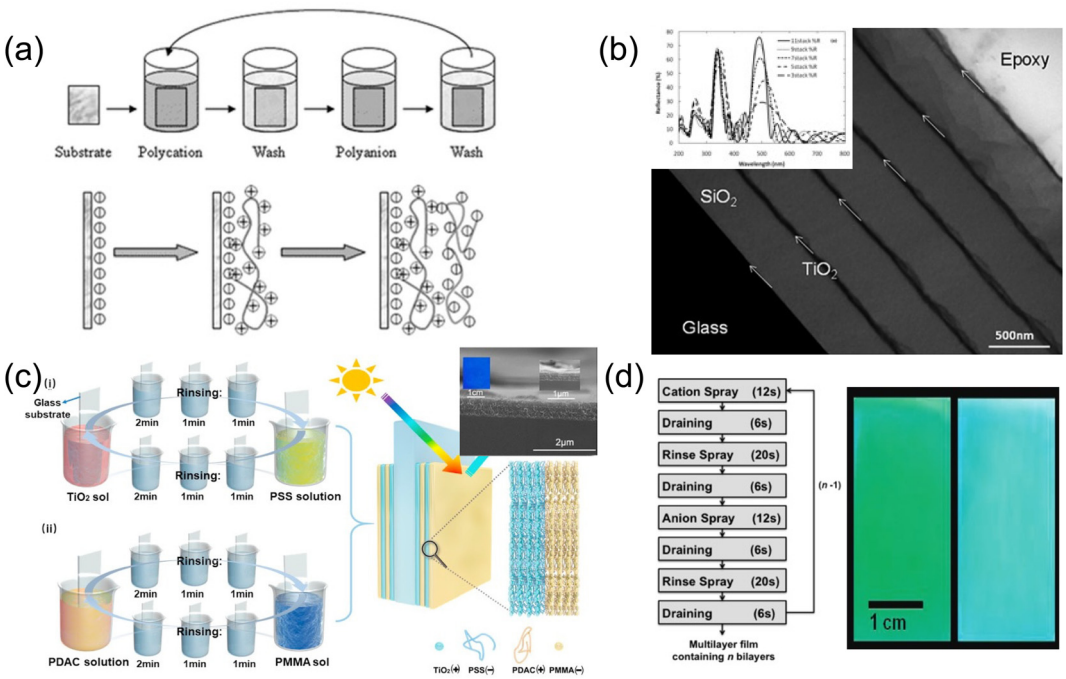

Fig. 12 (a) Schematic illustration of a LbL process where alternative coatings of polycation and polyanion are implemented. [Reproduced from ref. 127, with permission from American Chemical Society, Copyright 2020]. (b) SEM and reflection spectra of PAH-SiO_2 or TiO_2-PVS multilayers. [Reproduced from ref. 129, with permission from Royal Society of Chemistry, Copyright 2009]. (c) Hydrophobic Bragg reflector made of PMMA particles with LbL coating. [Reproduced from ref. 130, with permission from Elsevier Publishing Group, Copyright 2021]. (d) Spray coating LbL TiO_2/SiO_2 Bragg stacks featuring large area uniform structural colors. [Reproduced from ref. 131, with permission from American Chemical Society, Copyright 2011].

cycles of cation spray-draining-rinse spray-draining-anion spray-draining-rinse spray-draining. Compared to a similar dip-coated structure, the spray coating method significantly reduces a bilayer coating time from 36 min to 90 s while preserving color uniformity and smooth interface between layers. An iridescent 11-stack green-cyan structural color film (Fig. 12d right) with high reflectivity over 90% was demonstrated after calcining the LbL film under 550 °C.

2.2.2. Structural colors from physically additive deposition. Considering the LbL bilayer thickness only features a few nanometers, it would usually take a very time long to go over hundreds of cycles in order to reach a desired layer thickness. Instead of using electrostatic interaction between charged layers, directing deposition of materials in an additive way with quick solvent removal is proved to be a more efficient way of building structural color stacks.

Spin coating provides an effective way of rapid solvent removal through centrifugal force, leaving a thin layer of material on surface. The thickness of the spin-coated film can be tuned by solute concentration, solvent evaporation rate and spin rate. Silvia *et al.* has demonstrated a 1-D Bragg reflector[132] with alternative SiO_2/TiO_2 layers directly out of SiO_2 and TiO_2 nanoparticle solutions (Fig. 13a). Methanol was chosen as a cosolvent with water for the nanoparticle solutions to prevent coagulation and enhance the solvent volatility during spin-coating. The as-spun film thickness ranges from 40–200 nm in accordance with nanoparticle solution concentration from 1–6 wt%. Subsequent layers can be coated continuously without further stabilization. The entire Bragg stack can therefore be built within a few minutes followed by annealing to stabilize the layers mechanically. Infiltration of polymer materials such as polydimethylsiloxane (PDMS) into the Bragg stack further enables the making of a flexible structural color[133] (Fig. 13b). In addition to inorganic Bragg reflectors, polymeric materials[134] are excellent thin film candidates for direct spin-coating. Several examples using high index polymers like hyperbranched polyvinyl sulfide,[135] poly(*N*-vinylcarbazole),[136] *etc.* have been used in a full-polymer Bragg reflector through spin coating and feature brilliant structural colors.

2.2.3. Structural color from sol–gel chemistry. In addition to direct deposition of desired materials (as shown in Sections 2.2.1 and 2.2.2), thin film coating process can be coupled with chemical reaction, which facilitates film formation during the coating process. Compared to direct deposition methods where desired materials are synthesized, prepared, and stabilized in advance, incorporating film formation chemistry into the coating process significantly reduces cost and time in material preparation and maintenance.

For dielectric layer coatings, metal alkoxides are the most common oxide precursors, where they can be easily dissolved in various types of solvents and are ready to use. When water is introduced, metal alkoxides undergo hydrolysis to form metal hydroxides, which then condense into metal oxides. Thus, the sol–gel process provides a universal method for film formation from a variety of dielectrics. The coating conditions determine the sol–gel kinetics and thus the film properties including thickness and density, and composition can be changed accordingly. One strategy of depositing SiO_2/TiO_2 multilayer Bragg reflector utilizes an electro-assisted sol–gel process (Fig. 14a), where a bias is applied to a conductive substrate (cathode) to reduce water to OH^- and create a basic local environment.[137,138] The sol–gel condensation reaction kinetics are then boosted, triggering deposition of the oxide material onto the substrate. The deposited layer thickness is determined by the applied bias and deposition time. The as-deposited film, after being withdrawn from the solution and dried, is ready for the deposition of the next layer.[139] The multilayer film shows fairly smooth interfaces as well as a decent stop-band. Similarly, spin-coating of titanium alkoxide is adopted in structural colored photovoltaic cell fabrication to balance the color performance and PV cell efficiency.[140] Rapid spinning of the titanium alkoxide solution triggers the TiO_2 condensation as solvent evaporates. The as-spun film thickness is thus determined by the spin-rate as well as the evaporation rate.

However, due to the internal stress buildup inside the sol–gel film with increased thickness, overall stack thickness is

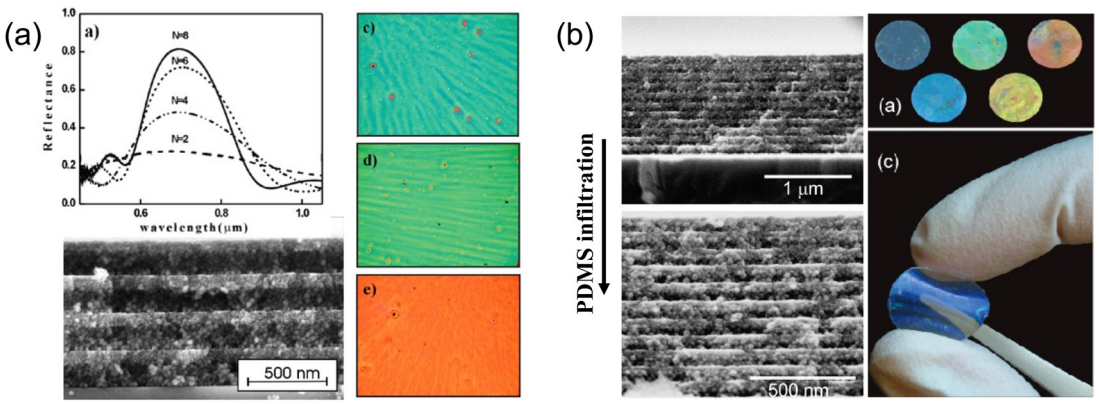

Fig. 13 (a) Optical and SEM image of spin-on alternative SiO_2/TiO_2 layers of Bragg stacks and their reflection spectra. [Reproduced from ref. 132, with permission from American Chemical Society, Copyright 2008]. (b) PDMS infiltrated inorganic Bragg reflector featuring flexible structural colors. [Reproduced from ref. 133, with permission from American Chemical Society, Copyright 2010].

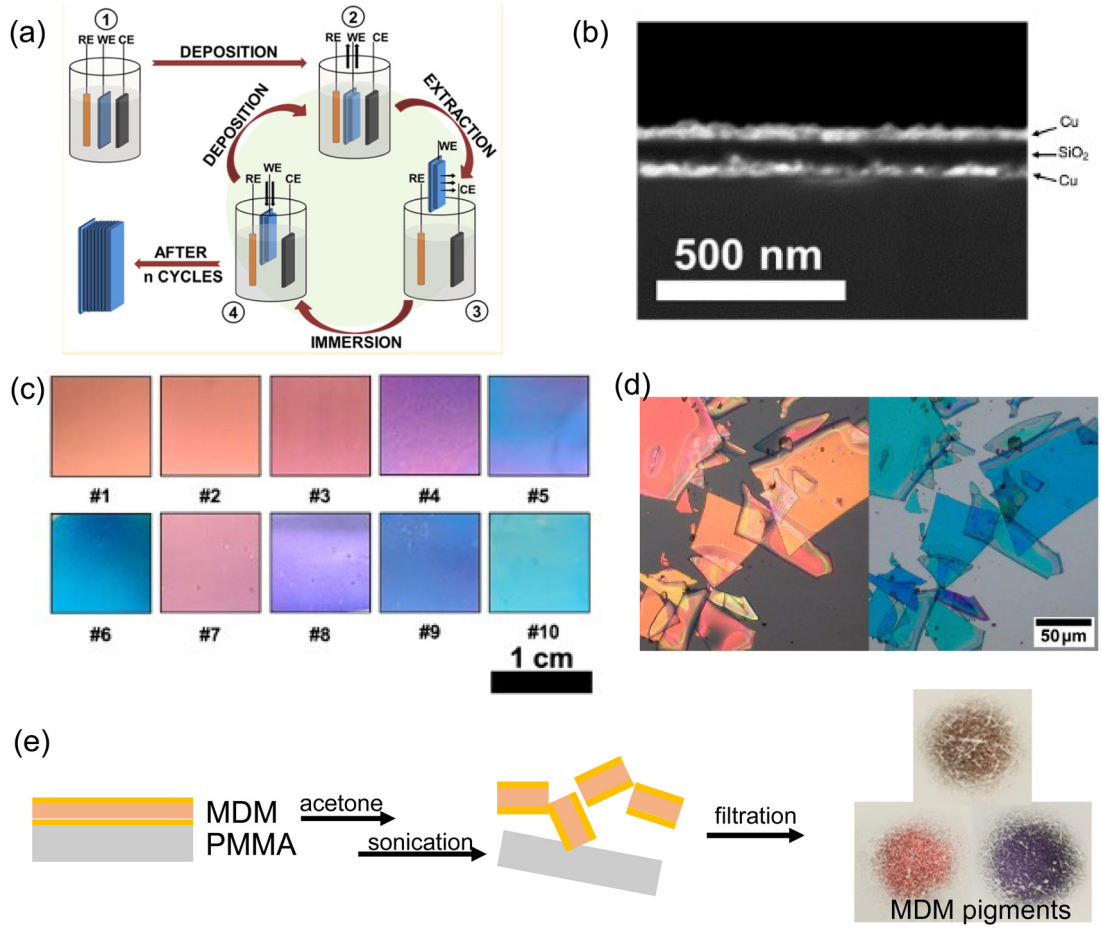

Fig. 14 (a) Schematic illustration of electro-assisted sol–gel process. [Reproduced from ref. 137, with permission from American Chemical Society, Copyright 2017]. (b) Cross-section SEM showing F–P type ($Cu/SiO_2/Cu$) structural color and (c) their brilliant color appearances.[141] (d) Cracked TiO_2/SiO_2 Bragg reflector flakes due to internal sol–gel process stress.[142] (e) MDM structural color pigments lifted off by sonication.

usually limited to a few micrometers to avoid cracking or delamination. Therefore, though sol–gel based thin film coating is very effective with oxide films tens to hundreds of nanometers thick, it is not suitable for complicated photonic structure fabrication. However, high-performance structural colors can be produced with structures simpler and thinner than photonic crystals or Bragg reflectors. The Fabry–Perot (F–P) cavity structure has less than four layers and has been explored as a popular candidate. A lossy cavity is required to absorb the resonant light energy and leaves a resonance dip in the reflection spectrum, giving subtractive colors like cyan, magenta, and yellow. For example, we have demonstrated a tri-layer metal-dielectric-metal (MDM)-type F–P cavity fabricated using a full solution process. The fabrication method combines electroless deposition of metal layer (Cu) with a sol–gel coated SiO_2 or TiO_2 deposited through dip-coating.[141] Various iridescent colors from orange to cyan have been produced with a total stack thickness under 200 nm (Fig. 14b and c). Hence, dip-coating of the sol–gel film provides a decent amount of control in film thicknesses by varying the precursor solution concentration or the withdrawal rate. Notably, such full solution-processed MDM method ensures solution compatibility across all dielectric and metal layers without compromising layer quality. The coated film shows a low surface roughness of 1.8 nm across a centimeter scale sample surface. Further, we have demonstrated that a modified F-P layer structure with the sequence of high-RI/low-RI/Absorber (HLA) could also produce brilliant and vivid structural color with proper balance between the radiative and absorptive decay rate of the F–P cavity.[143] With a similar sol–gel process, $TiO_2/SiO_2/Si$ or $ZrO_2/SiO_2/Si$ stacks can be dip-coated from metal alkoxide solution. These HLA structural colors could easily span the entire CMY space by varying the dielectric layer (*i.e.* high RI or low RI) thickness.

2.2.4. Multilayer structural color pigments. In addition to structural color coating on bulk substrate, breaking these multilayer stacks or films into flakes or pigments is highly desired for incorporation into normal paints. With structural color pigments oriented in all directions, it averages out the angle-dependent effect of a multi-layer structure while keeping a pearlescent visual effect, *i.e.* luster. Moreover, these colored pigments could be incorporated into polymeric binders for easy painting, allowing for application on a wide variety of surfaces. One straightforward way of fabricating structural color pigments is by directly breaking down the multilayer film

fabricated on a bulk substrate. In the case of a sol–gel TiO_2/SiO_2 Bragg stack obtained through spin-coating, the internal stress could naturally cause the film to crack and break into micrometer-scale flakes (Fig. 14d).[142] The cracked pigments show a more lustrous diffusive color with a broader reflection peak due to the random orientation of the flake surface. We have also demonstrated a lift-off method for F–P type of structural color fabrication where the MDM stack is being fabricated on top of a sacrificial PMMA layer, followed by a sonication of substrate in acetone. The MDM structural color flakes can then be obtained through simple filtration and drying (Fig. 14e).

However, the fragmentation method efficiency and yield are insufficient for large-scale production. A more practical way of structural color pigment fabrication involves an additive method to coat flake substrate bottom-up. Mica, a smooth sheet layered silicate, is widely adopted as a perfect flake substrate. Over the past decades, various metal oxides, including Fe_2O_3, TiO_2, $Pb(OH)_2$, $PbCO_3$, BiOCl, $(Sn,Sb)O_2$, *etc.* have all been demonstrated as good candidates for pearlescent mica pigment synthesis.[144,145] Deposition of a metal salt precursor is trigged under carefully chosen conditions to selectively deposit onto the activated mica surface and avoid bulk precipitation. The filtered pigments are then calcinated under high temperature for dehydration and crystalized into metal oxides.

Solution-processed multilayer coating offers a simple and intuitive layer by layer method for multilayer film color production. While it mimics the thin film deposition commonly takes place in vacuum chambers, it allows the quick fabrication of multilayer structure under ambient condition. With careful engineering controls, large scale uniformly colored film can be fabricated continuously with multiple coatings. Hence the cost is greatly reduced by getting rid of the harsh fabrication environment and the cost in tool maintenance. One challenge still presents in the complexity of chemistry involved in solution-processed multilayer coating. In addition to the internal stress caused by different material lattice matching (*i.e.* usually a concern in vacuum-based deposition), chemical compatibility between multilayer coatings as well as their compatibility with substrate is of great concern during fabrication. Reliable and compatible chemical coating recipes are highly desirable in future research and development.

2.3. Structural color produced from electrochemical methods

Electrochemical methods are another way to shape the structure of thin films. It is well-known that anodization of aluminum surfaces leads to the formation of cylindrical holes with honeycomb structures.[146] The aluminum surface is oxidized in acidic aqueous solution under high voltage and the radial current distribution leads to a cylindrical hole throughout the oxidized layer. This technique has been widely adopted in modern aluminum surface coloration where dye pigments are encapsulated inside the anodized aluminum oxide (AAO) holes. Since the hole size is directly proportional to the current density across the surface, Liu *et al.* has designed a stack of AAO layers with different refractive indexes,[147] mimicking a 1D Bragg-type reflector. A pulsed anodization of aluminum is carried out. By varying the current passed through the aluminum surface with different pulse duration, AAO layers with various porosity and thickness are formed (Fig. 15a). The refractive index of each porous layer can be approximated with a linear combination of the RI from Al_2O_3 and air by the fill fraction. The resulting multilayer stack shows brilliant color in both transmission and reflection due to the formation of a high contrast, wide stopband within the visible range. Furthermore, a highly ordered porous AAO film can be obtained with a novel self-ordering electrolyte, namely etidronic acid.[148] The aluminum surface is anodized under a self-ordering voltage (210–270 V for etidronic acid) followed by selective dissolution of aluminum oxide in CrO_3/H_3PO_4 solution. In contrast to the AAO Bragg stack, the structural color produced with self-ordering anodization comes from a 2D photonic crystal. Large hole sizes from 500–800 nm can be obtained, giving rainbow color from red to violet (Fig. 15b).

Other metals like platinum, titanium, silicon *etc.* can be anodized as well. Due to the high refractive index of TiO_2, structural colors from anodized TiO_2 on Ti can be readily produced. Fig. 15c demonstrates structural color produced *via* Ti anodization under different anodization times.[149] The SEM images revealed changes to the TiO_2 surface morphology where indentation and protrusions inside the lamellar structure are critical for color production. More ordered TiO_2 arrays (Fig. 15d) were grown directly on top of the Ti sheet through two-step anodization.[150] A potential of 30–75 V was applied in the first anodization step, producing a rough and irregular TiO_2 honeycomb structure. The TiO_2 layer was then removed with a sticky tape, leaving an array of concave cavities on the Ti sheet surface. A second anodization step was then carried out, forming hierarchical TiO_2 bowl arrays. A rainbow color can be visualized by increasing the air cavity size inside the bowl array. The reflection spectrum features two broad stop-bands (Fig. 15e) where two peaks correspond to the first and second order diffraction from the periodic TiO_2 bowl surface respectively.

Electrophoretic deposition (EPD), on the other hand, utilizes electrostatic force to move charged particles towards the electrode surface for deposition. Negatively charged SiO_2 nanoparticles pre-synthesized by sol–gel chemistry are forced to deposit onto an ITO glass anode under applied voltage.[151] A well-ordered PhC was formed with close-packed SiO_2 particles under low EPD voltage ($\sim$5 V, 25 min), while an amorphous PhG was obtained once the EPD voltage increased to 90 V (1 min). The difference in the resulting structural color could be clearly seen by the change in color iridescence and angle-resolved spectra. Compared to the convective deposition method of PhC or PhG described in Sections 2.1.1 and 2.1.2, EPD uses a much shorter deposition time to deposit conformal and uniform structural colors across curved surfaces (Fig. 16a). Another example[152] uses EPD of pre-synthesized polystyrene (PS) onto carbon fiber to give core–shell type structural color fibers with colors in red, green and blue (Fig. 16b). The flexibility and relative high throughput of the EPD structural color fiber shows promising applications in developing dye-free fabrics or textiles.

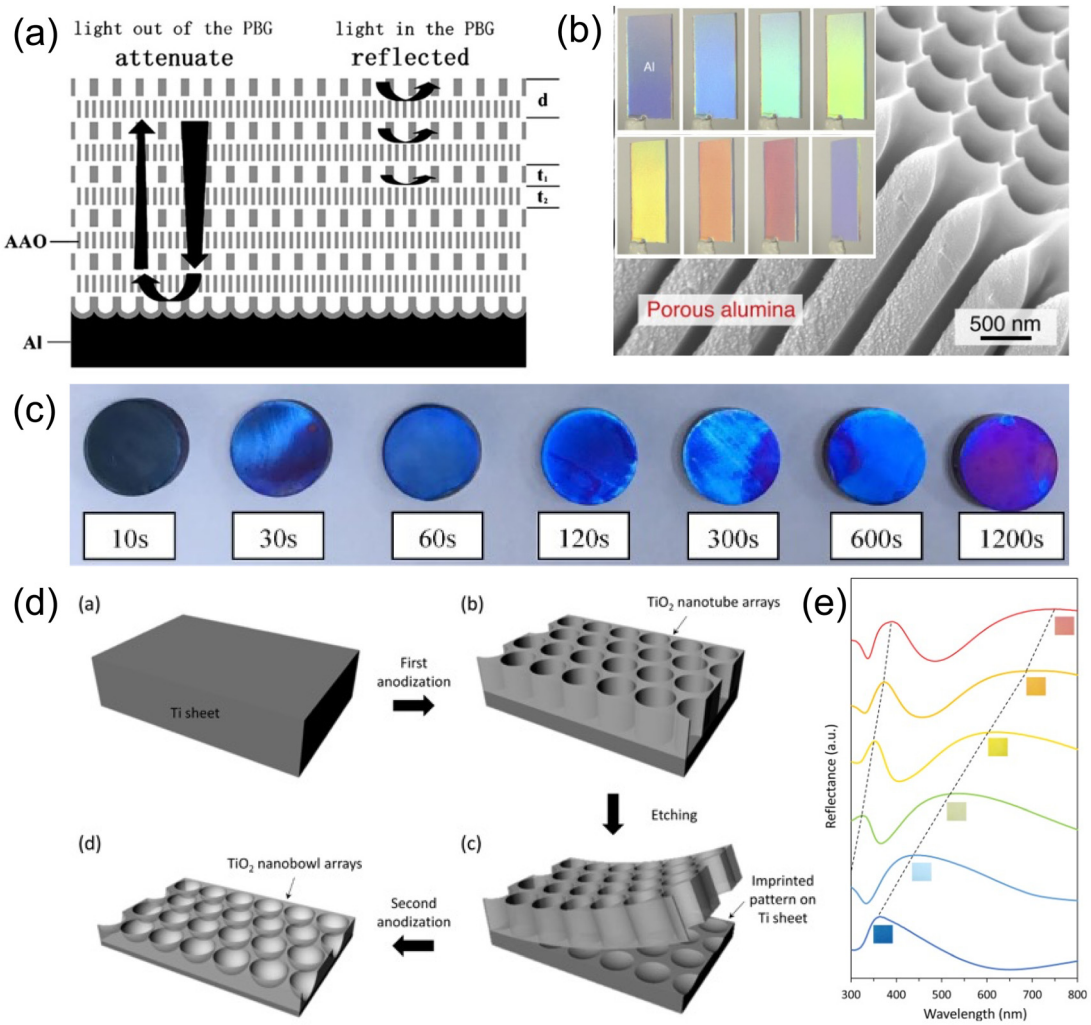

Fig. 15 (a) Schematic illustration of porous AAO Bragg stack with pulsed anodization of aluminum. [Reproduced from ref. 147, with permission from Elsevier Publishing Group, Copyright 2011]. (b) Structural colored AAO photonic crystal from self-ordered anodization process. [Reproduced from ref. 148, with permission from Elsevier Publishing Group, Copyright 2015]. (c) Gradual change of color in anodized titanium film over various anodization times. [Reproduced from ref. 149, with permission from Elsevier Publishing Group, Copyright 2023]. (d) A schematic diagram demonstrating the fabrication of TiO_2 nanobowl array on titanium film and (e) their corresponding refraction spectra. [Reproduced from ref. 150, with permission from American Chemical Society, Copyright 2016].

In contrast to the process of anodization or EPD, where a large voltage is required to induce electrochemical responses, electrochemical deposition uses a very small voltage to trigger a chemical reaction at the electrode–electrolyte interface for layer deposition. Electrodeposition of F–P cavity-type structural color (Fig. 16c) has been demonstrated with an Au/Cu_2O/Au trilayer stack on a heavily n-doped Si substrate.[153] As a reduction potential was applied to the cathode, the positively charged metal ion (*i.e.* Au(III)) is reduced into its metallic state on the Si substrate. Similarly, Cu_2O is reduced from a copper citrate complex by carefully controlling the solution pH and applied potential to prevent over reduction into metallic copper. The top Au layer is carefully deposited with a solution pH ~10–11 compatible with the Cu_2O layer while applying a relative low reduction potential to avoid aggressive hydrogen evolution, which can peel off the underlying layers. Shiny yellow, magenta, and cyan colors are produced (Fig. 16d) conformally on both flat Si substrates and curved stainless steel spoon surfaces, demonstrating promise in coating objects with complex geometries.

In brief, electrochemical methods provide new pathways toward structural color fabrication. Chemical reactions are triggered at the electrode–electrolyte interface with the flow of electrons gauged through the voltage applied. With the ability of both 2D growth thin film growth and 3D sculpting of the surface, electrochemical methods unlock the various possible photonic structures. Moreover, with careful control on the surface current distribution, the film thickness can be tuned to achieve either uniform or gradient color appearance. Thus allowing special visual effect to be produced with one deposition. However, the limitation with electrochemical methods is quite obvious where a conductive substrate is always required. The process window of electrochemical methods is another concerned due to side reaction and layer compatibility with in the electrolyte.

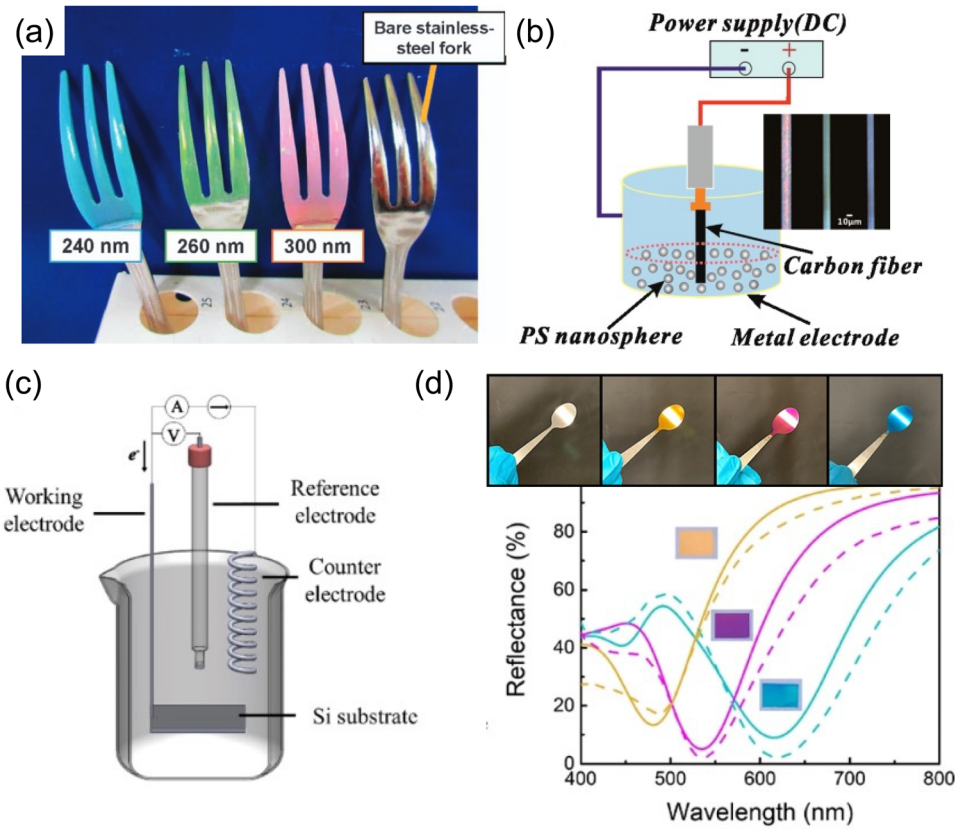

Fig. 16 (a) Structural colored forks coated with electrophoretic deposition of SiO_2 nanoparticle on curved surfaces. [Reproduced from ref. 151, with permission from Nature Publishing Group, Copyright 2017]. (b) Photonic crystal of PS particles deposited by EPD on carbon fibers. [Reproduced from ref. 152, with permission from American Chemical Society, Copyright 2013]. (c) A schematic illustration of an electrochemical deposition setup. (d) Electrodeposited Au/Cu_2O/Au structural color on curved stainless steel spoon surface and their corresponding reflection spectra. [Reproduced from ref. 153, with permission from American Chemical Society, Copyright 2019].

2.4. Structural color from particles

2.4.1. Color from plasmonic resonance. Structural color from plasmonic nanoparticles has been widely used for coloration for centuries before the underlying mechanism was elucidated in recent decades. Starting from the famous 4th century Lycurgus cup to stained glass, plasmonic nanoparticles have played an important role in color decoration. Metal nanoparticles such as gold, silver *etc.*, possess strong localized surface plasmon resonances in the visible spectrum giving various colors depending on particle size, shape, and surface functionalization. In recent decades, scientists have mastered every aspect of nanoparticle synthesis, enabling a well-controlled color appearance. Common spherical solution-based nanoparticle synthesis features a homogenous or heterogenous nucleation and growth process. A reductant or nanoparticle seed is added to trigger the nucleation process, followed by a gradual color change of the solution. The final size of the plasmonic nanoparticle depends on the reaction time, solution concentration, reactant ratio, *etc.* Silver[154] and gold nanoparticle[155,156] feature plasmonic absorption peaks around 400 nm and 520 nm respectively, giving a bright yellow or burgundy red color appearance. While spherical nanoparticles do not change their absorption band or color dramatically with size, the addition of certain ligands can promote anisotropic by promoting specific facet growth. Compared to spherical nanoparticles, anisotropic nanoparticles (typically nanorods[157–160] and nanodisks[161,162]) show significant shifts in absorption peak wavelength (the longitudinal plasmonic band) with changes to size or aspect ratio and are thus capable of generating colors across the visible spectrum.

Though nanoparticle solutions alone show fascinating transmissive colors, immobilization of these nanoparticles further expands their use in plasmonic structural colors. Over the past five years, it has been shown that the incorporation of disordered nanoparticles into various photonic structures can lead to very different colors from when a continuous metal layer is used. The optical property of the nanoparticle layer evolves with changes to layer morphology, giving distinctive color appearances. As shown in Fig. 17b, a discontinuous metal layer (*i.e.* metal nanoparticles) gives rise to primary reflective peaks in a F–P type structure,[163–166] polarizonic colors (named after electronic oscillation at optical frequency) on metal substrate,[167–169] gap-plasmon-resonance color with ultrathin dielectric layer[170,171] *etc.* These initial attempts of nanoparticle deposition require quite special deposition techniques including arc plasma deposition, cluster beam deposition, e-beam evaporation, *etc.*, making them far from practical for mass production. However, immobilizing solution-based nanoparticles is a promising pathway for cost-effective plasmonic structural color fabrication.

One straightforward solution deposition method utilizes the electrostatic attraction of charges between nanoparticle surface and substrate.[173,174] As shown in Fig. 17a, gold nanoparticles of desired size capped with negatively-charged citrate ligands were pre-synthesized in aqueous solution. On the other hand, positive charges were functionalized onto a silica-based substrate through silanization with (3-aminopropyl)triethoxysilane (APTES). A gold nanoparticle monolayer was adsorbed onto the silica surface after immersing the substrate into the nanoparticle solution. The nanoparticle surface density can be well controlled (Fig. 17b) by immersion time, ionic strength and nanoparticle solution concentration. In another example, oleylamine-capped silver nanocubes were spin coated onto an APTES-treated SiO_2/Ag substrate.[172] Vivid colors were produced with a wider absorption stopband (Fig. 17c) than a sintered or smooth thin silver film. Another method of nanoparticle immobilization is *via* direct growth of nanoparticles on substrate surface. A seed layer is first required as a nucleation and growth center. Electroless deposition of metal provides a perfect method to implement this process. Fig. 17d records a time-evolution of copper electroless plating in both surface morphology and color appearance.[141] The top copper layer first forms discrete particles (30 s), then grows into islands (1 min), and finally overlaps with each other (2 min). A particulate morphology is always observed even with extending deposition time ($\geq$5 min) due to the repetitive growth pattern, *i.e.* particle-island-film. Hence, the copper film reflectivity increases with deposition time while always featuring low reflectivity in lower wavelengths compared to a vacuum-deposited copper film. With short electroless deposition times of copper on top of SiO_2/Cu surface (*i.e.* F–P type cavity), a series of additive colors with reflective peaks can be clearly observed (Fig. 17e and f). As in the case of gold nanoparticles, the addition of chloroauric acid ($HAuCl_4$) and hydroxylamine (NH_2OH) facilitates the growth of the seed layer into larger nanoparticles. Note that the pre-deposited seed layer catalyzes the sluggish reduction reaction kinetics between $HAuCl_4$ and NH_2OH, thus enabling *in situ* growth of gold nano-domains on the surface.[175–178]

2.4.2. Color from collective particle scattering. Light resonance within dielectric particles from multipole radiation are well understood by Mie theory.[179] In addition, structural colors can be produced with a collective dielectric particle scattering of light. Wu *et al.* has found that spherical dielectric particles larger than 200 nm with medium refractive index (n = 1.7–3.0, such as ZnS, ZnO *etc.*) strongly scatter certain visible wavelengths.[180] As these particles tend to aggregate in an ordered way, the electric dipoles of aggregated particles approach each other and enhance the scattering peak *via* dipole interference (Fig. 18a). Simulation results indicate that a 6–9 nanoparticle aggregate shows the most pronounced increase in scatting intensity, or namely nanosphere-aggregation-induced reflection (NAIR). ZnS particles were synthesize *via* a typical precipitation method where thioacetamide is used to precipitate zinc ions under the protection of poly(4-vinylpyridine) (PVP). The as-formed suspension was then casted and dried through an infiltration-driven nonequilibrium colloidal assembly method[181] where locally ordered aggregation structure is preserved (Fig. 18b and c). Rainbow colors featuring CMYK were produced by changing the particle size along with appropriate mixing of particles of different sizes. Rapid inkjet printing is demonstrated to show the potential of NAIR with its maximum resolution of 25 000 dpi. Further engineering of the particle refractive index, size and interparticle distance allows for separation and tuning of the multipole contribution in dielectric particle scatting (in this case, the electric dipole ED and electric quadrupole EQ), giving a rarely observed red color. Disordered ZnO particle aggregates can be obtained *via* dip-coating, where the surface coverage and therefore interparticle spacing can be well controlled.[182] Several potential applications of NAIR have been demonstrated in the field of colored photovoltaic cells,[35] automobile paints,[183] anticounterfeiting[184] *etc.* As a final note for this section, Mie resonance induced color is only observable for particles of relatively high refractive index. Low index particles,

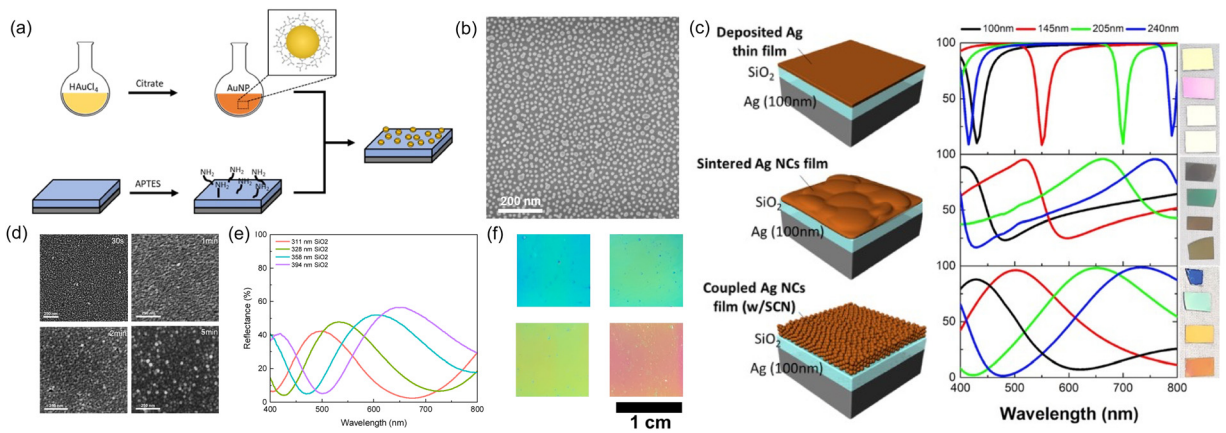

Fig. 17 (a) Schematic illustration of gold nanoparticle synthesis and immobilization/deposition on substrate. (b) SEM image of gold nanoparticles deposited on surface. (c) Schematic configurations, absorption and reflection of various Ag/SiO_2/Ag structural color. [Reproduced from ref. 172, with permission from American Chemical Society, Copyright 2019]. (d) SEM images showing the evolution of electroless deposited copper on substrate surface. (e) Reflection spectra and (f) color appearance of Cu nanoparticle/SiO_2/Cu structural color. [Reproduced from ref. 141, with permission from Wiley-VCH Verlag GmbH & Co. KGaA, Weinheim, Copyright 2013].

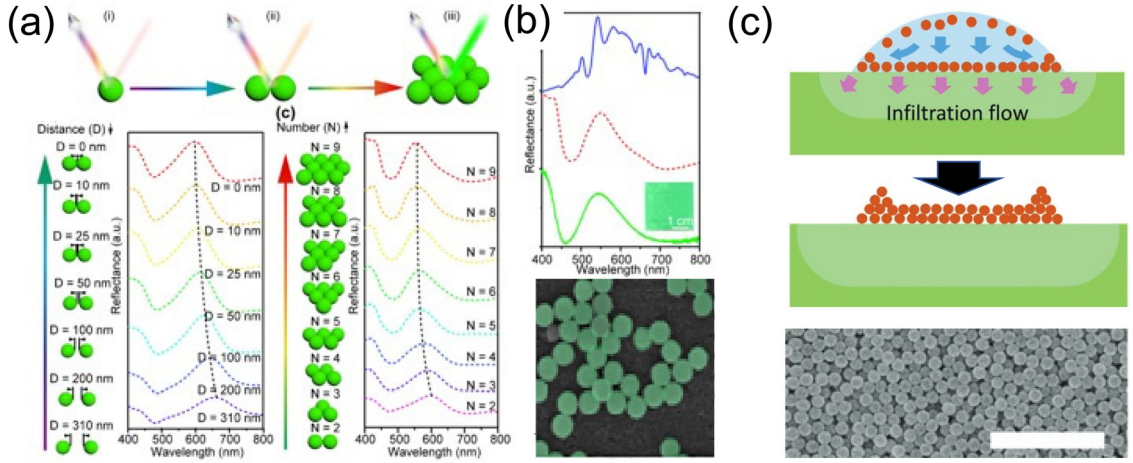

Fig. 18 (a) Schematic illustration of NAIR and their reflection spectra with various configurations. (b) Simulated reflection spectrum of aggregates constructed of nine 310 nm dielectric spheres (red dotted line), experimental reflection (green solid line), and dark-field reflection (blue solid line) spectrum of aggregates constructed of 310 nm ZnS spheres (green solid line). The inset is the digital image of this aggregate and their false colored SEM image. [Reproduced from ref. 180, with permission from American Chemical Society, Copyright 2020]. (c) Schematic illustration of infiltration-driven nonequilibrium colloidal assembly and the resulted SEM. Scale bar: 2 μm. [Reproduced from ref. 181, with permission from Wiley-VCH Verlag GmbH & Co. KGaA, Weinheim, Copyright 2018].

e.g. SiO_2, only produce broad resonance that is hardly visible. Zhou *et al.* reported that, after coating with a thin metal cap, the single particle resonance becomes highly pronounced and the resulting color strongly correlates with the particle size.[185]

With confined space, nano-/micro-particle-derived structural colors distinguish themselves from self-assembled structural colors, where colors are produced within one single particle or particle cluster instead of bulk assemblies. Hence, particle-derived colors never suffer from assembly uniformity or defects. Besides, resonance inside particles could be added to other structural color platforms to produce richer color appearance. However, note the scattering nature of these colored-particles would likely lead to a more diffusive color appearance, special treatment or preparation methods are needed to produce bright reflective color.

3. Tunability of solution-based structural color

3.1. Responsive structural color *via* spatial tuning

3.1.1. Mechanochromic structural color. Mechanical deformation, *e.g.* strain, compression, bending, or torsion, is the most direct way to change the spacing of color generating structures, providing direct readout of a material's mechanical response. Materials used in mechanoresponsive structural color must be able to deform and recover through their dynamic range. Periodic nanostructures or photonic crystals, such as inverse opals, are effective here when prepared from mechanically robust and flexible polymers. Wang *et al.* created a structurally colored hydrogel patch for wound management capable of releasing drugs under electrical stimulation[186] (Fig. 19a). The color comes from the inverse opal structure whose spacing changes under deformation, providing a colorimetric readout to mechanical perturbation, thereby warning the user against putting too much strain on a wound. Combining this effect with swelling (as described in Section 3.1.3), Zhang *et al.* developed a trilayer actuator gripper (Fig. 19b) whose open and closed states are visualized using an incorporated inverse opal hydrogel layer.[187] Consisting of poly(acrylic acid-*co*-acrylamide) (PAAc-*co*-AAm) and poly(*N*-isopropyl acrylamide) (PNIPAAm) joined by an inverse opal scaffold, the hydrogel actuates through swelling of either the PAAc-*co*-AAm or PNIPAAm layer, which changes the spacing of the opal and therefore its color. The gripper is green in the open state and red in the closed state, providing visual feedback to actuation. Departing from opals, Goodling *et al.* microstructured an elastomer surface with repeating domes or wells from self-assembly of glass particles at an oil–water interface[188] (Fig. 19c). Both dome-patterned and well-patterned materials have structural color from the total internal reflection of light inside the domes and wells. Stretching the pattern changes the path of the reflected light, thus changing the color. Through the well-defined optics of photonic structures, any material with sufficient mechanical robustness can be used to create mechanoresponsive structural color.

Strain can also be used to modulate the spacing of structurally colored liquid crystals (LCs). Though liquid crystal-based structural color is difficult to fabricate into free-standing materials, several efforts have been made to enable sufficient robustness for use in mechanoresponsive sensing, such as supporting the LC films on a more robust polymer, incorporating them directly into the polymer backbone, or encapsulation by a more robust polymer. Kim *et al.* developed a system for colorimetric pressure readout utilizing a crosslinked copolymer elastomer incorporating a chiral nematic LC[189] (Fig. 19d). The LC was allowed to self-assemble and stabilize, and the resulting film was mounted to a PDMS film that was then mounted to an air inlet. Under applied air pressure and therefore plane stress,

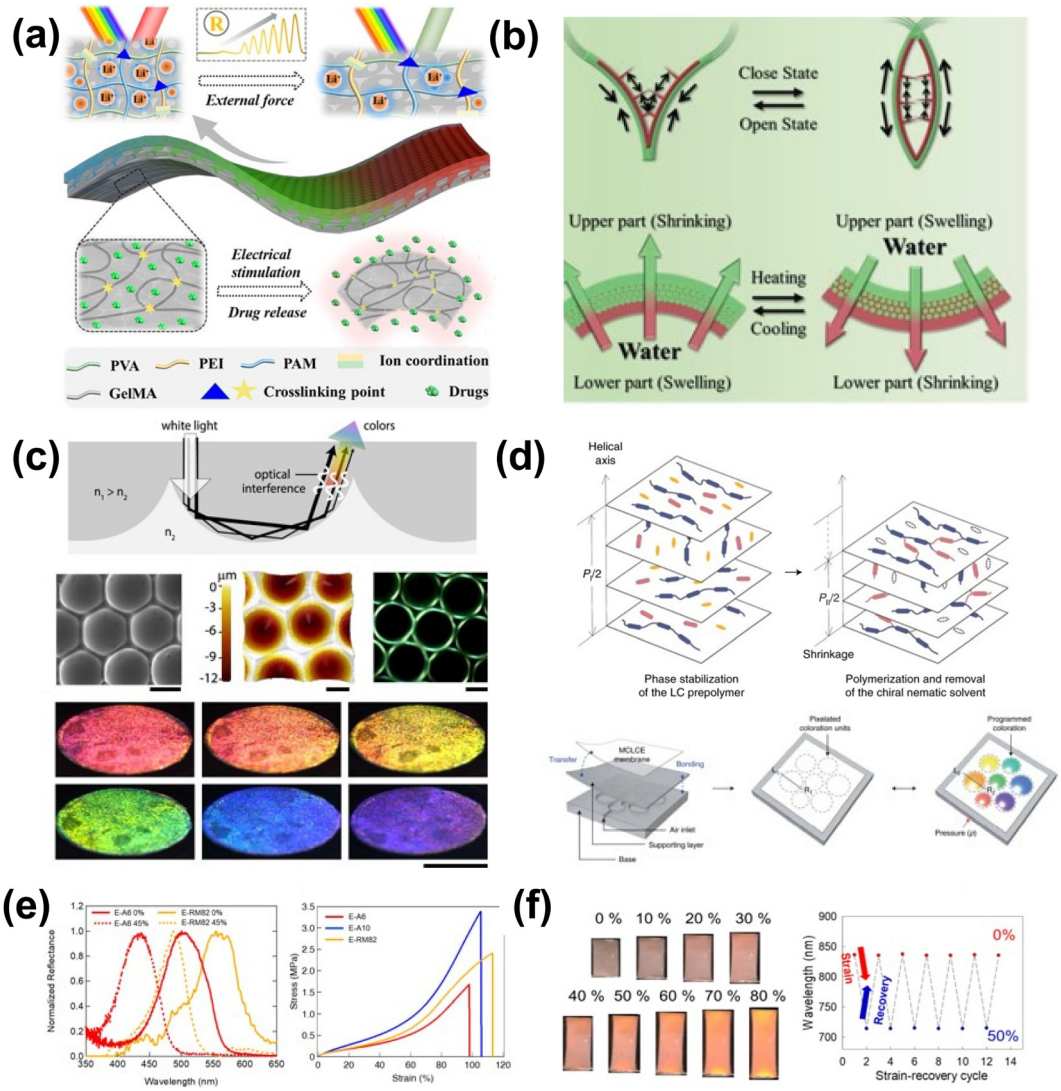

Fig. 19 (a) Schematic diagram of the inverse opal scaffold-based structural color ionic hydrogel patch encapsulating drugs where drug release is triggered by electrical stimulation. [Reproduced from ref. 186, with permission from American Chemical Society, Copyright 2023]. (b) Schemes of the bilayer structural color hydrogel with multienvironment survivability. [Reproduced from ref. 187, with permission from Wiley-VCH Verlag GmbH & Co. KGaA, Weinheim, Copyright 2019]. (c) Microwells and domes with structural coloration appearance from total internal reflection. [Reproduced from ref. 188, with permission from American Chemical Society, Copyright 2020]. (d) Programmable structural coloration of membranes based on Poisson effect. Schematic diagram showing the pixelated structural coloration platform, consisting of a base with air channels, a supporting layer and a structural color membrane. [Reproduced from ref. 189, with permission from Nature Publishing Group, Copyright 2022]. (e) Reflectance spectra (left) of crosslinked LC elastomers under tensile strain of 0% (solid line) and 45% (dashed line). Stress–strain curves (right) of the chiral nematic liquid crystal elastomers. (f) Photographs of the chiral nematic liquid crystal elastomer under applied tensile strains of 0–80% and mechano-optical stability of the chiral nematic liquid crystal elastomer film during compressive/tensile strain cycles from 0% to 50%. [Reproduced from ref. 190,191, with permission from Multidisciplinary Digital Publishing Institute, Copyright 2021].

the LC's pitch changed, thus changing the observed color. Similarly, Ku *et al.* improved the response, thermal, and environmental stability of LC-incorporated polymer networks by introducing noncovalent intermolecular crosslinking *via* a cyanobiphenyl derivative capable of π–π and dipole–dipole interactions.[190,191] The resulting material exhibited fast mechanoresponsive optical behavior and recovery under applied and released tensile strain (Fig. 19e). Thus, the unique spatial properties of LC structural color can be modulated through deformation to create mechanoresponsive structural color (Fig. 19f), provided the LC is supported in a sufficiently robust material.

3.1.2. Thermochromic structural color. Temperature responsive structural colors utilize materials that undergo volume change under thermal transition to change the spacing of the color structures. Much of the multimodal research mentioned in this review incorporates thermal response by using a thermally responsive polymer or initiates thermal response using light or electrical stimuli. Due to the wide variety of thermally responsive polymers available, thermally

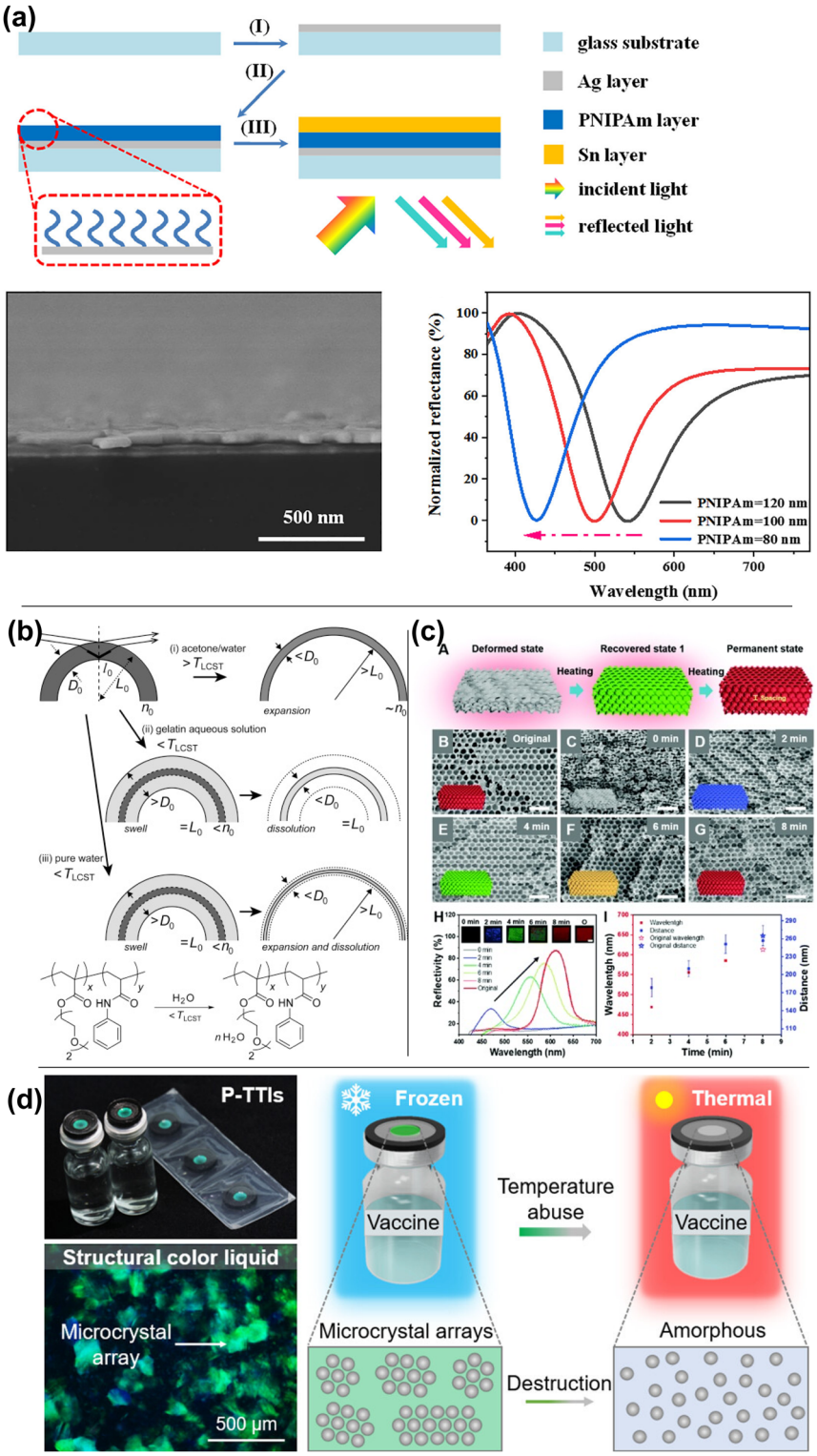

Fig. 20 (a) Schematic diagram of the preparation process, SEM image and reflection spectra of the proposed asymmetric F–P-type cavity for subtractive structural colors. [Reproduced from ref. 192, with permission from American Chemical Society, Copyright 2022]. (b) Schematic illustration of change in diameter 2L, thickness of the shell D, refractive index n, and the structural color of SCBs composed of poly(diethylene glycol monomethyl ether methacrylate)-*co*-poly(*N*-phenylacrylamide) (PDegMA–PNPAM) random copolymer under several stimuli. [Reproduced from ref. 193, with permission from American Chemical Society, Copyright 2018]. (c) Color tuning of the shape memory polymer-based PhC film through heat. SEM image showing the morphology change during deformation/recovery cycle along with the corresponding reflection spectra. [Reproduced from ref. 194, with permission from Royal Society of Chemistry, Copyright 2020]. (d) Illustration of thermal-triggered structural color destruction based on triggering agent-diffusion-induced irreversible disassembly of liquid colloidal PCs for indicating the time–temperature history of the vaccine. [Reproduced from ref. 195, with permission from American Chemical Society, Copyright 2023].

responsive systems are useful in realizing stimuli-responsive structural color. Frequently used are LCST polymers like poly(*N*-isopropyl acrylamide) (PNIPAAm), which undergoes deswelling and shrinkage when heated above 32 °C. Thus, PNIPAAm is widely used in creating thermoresponsive and multimodally responsive structural color. Liu *et al.* used PNIPAAm as a dielectric cavity in a silver/PNIPAAm/tin asymmetric Fabry–Perot cavity to create a temperature-responsive structural color film.[192] When immersed into warm water, the cavity shrinks, thus blue-shifting the reflection dip and observed color (Fig. 20a). This change is reversible when the film is immersed in cold water. Using a custom copolymer with tunable LCST, Higashiguchi *et al.* prepared structural color balloons[193] whose film thickness increases when swollen below the LCST temperature and decreases when deswollen above the LCST temperature (Fig. 20b), thus changing the path length of the reflected light. LCST polymers are a facile way of adjusting space in photonic structures; therefore, they are widely used in thermally responsive structural color.

Thermal transitions can be combined with other unique material properties, such as freezing point or shape memory, to trigger structural color changes. Using a thermally-triggered shape memory transition, Wang *et al.* created laser-writable photonic crystal paper using an inverse opal structured shape memory polymer.[194] The paper is held in its compressed, colorless state due to shape memory until it is written on using an NIR laser, upon which the shape memory is released and the photonic crystal is allowed to expand to its native state (Fig. 20c), which is red. The written color is controlled by the duration of the writing, with shorter periods resulting in blue-shifted colors. While heat can be used to recover color in thermoresponsive materials, it can be used to destroy color in others. To tackle the problem of time-temperature history indication during vaccine cold storage, Huang *et al.* developed a system where photonic microcrystal arrays wrapped in glycerol are exposed to a triggering agent consisting of a frozen aqueous glycol solution.[195] The glycerol-wrapped photonic crystals are sensitive to glycol concentration, which is controlled by the triggering agent's melting temperature (Fig. 20d). Upon melting of the triggering agent, the glycol mixes irreversibly with the glycerol-wrapped particles, thereby destroying them and their color. Thermal transitions can be applied to structurally colored materials in unique ways outside of using LCST polymer materials.

3.1.3. Solvent-responsive structural colors. Solvent-responsive structural color materials undergo a change to either the volume or refractive index from solvent infiltration or swelling. The sensitivity of observed color to film thickness or refractive index can discern solvents of similar refractive index, especially if certain solvents are selected for by employing certain chemical moieties found in swellable polymers. For example, hydrophilic acrylamides are particularly sensitive to water, while poly(propylene glycol) is easily swollen by cyclohexanone. For salt response, polyelectrolytes are employed. To respond to cyclohexanone, Sun *et al.* fabricated a cellulose nanocrystal (CNC) film blended with poly(ethylene glycol)–poly(propylene glycol)–poly(ethylene glycol) (PEG–PPG–PEG) copolymers.[196] To prevent water response, hydrophobic hexadecyltrimethoxysilane (HDTMS) is grafted on the outside (Fig. 21a). Cyclohexanone passes through the HDTMS layer and is absorbed by the PPG blocks, enlarging the distance between CNC layers, and causing a 107 nm red shift, observable as a blue-to-yellow color change. Of particular interest is the ability to discern solvents of

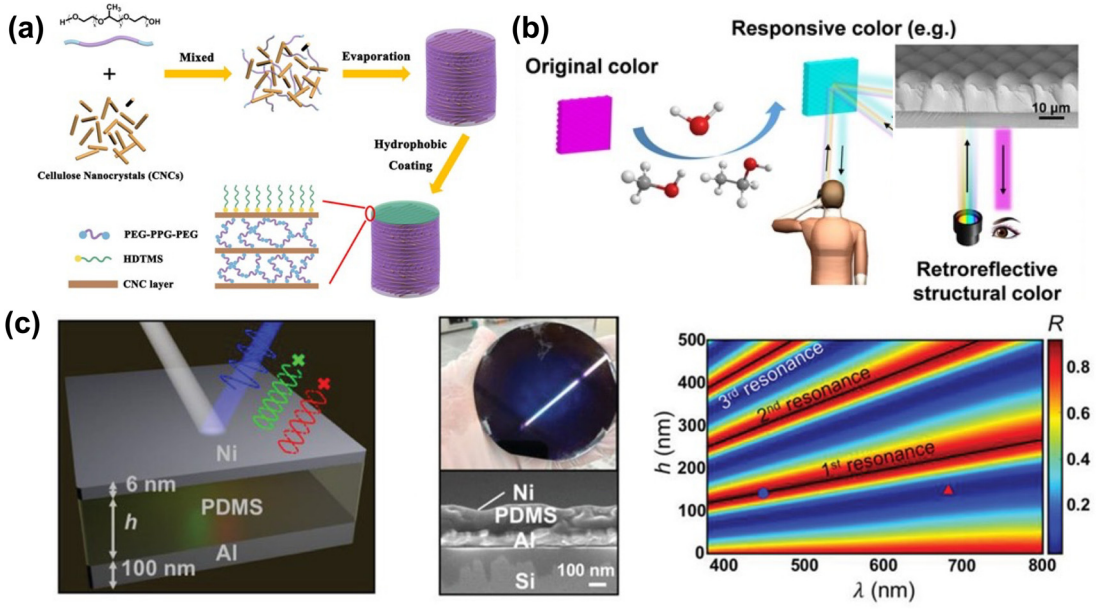

Fig. 21 (a) Schematic illustration for the preparation of hydrophobic CNC nanocomposite films with structural color. [Reproduced from ref. 196, with permission from American Chemical Society, Copyright 2020]. (b) The color of the egg-waffle film remains angle-independent when the retroreflective structural color film responds to varied humidity and organic vapors (methanol and ethanol). [Reproduced from ref. 197, with permission from Elsevier Publishing Group, Copyright 2021]. (c) Ni/PMDS/Al structural color demonstrating a solvent-responsive color change due to the volume change of the PDMS layer. [Reproduced from ref. 198, with permission from Wiley-VCH Verlag GmbH & Co. KGaA, Weinheim, Copyright 2019].

similar refractive index, such as methanol and ethanol. Ji *et al.* created a poly(acrylamide) (PAAm) organogel film capable of discerning methanol, ethanol, and humidity changes through volume swelling.[197] The film uses an "egg-waffle" pattern (Fig. 21b), similar to an opal, to generate structural color from retroreflection, total internal reflection, and interference. Combining both swelling and deswelling behavior, Kang *et al.* created a 1-dimensional photonic crystal from the self-assembly of a hydrophilic–hydrophobic block copolymer.[107] The hydrophilic layers are formed from a polyelectrolyte and swell in water depending on the salt content, thus changing layer thickness, refractive index, and therefore color (Fig. 9c). Geometric confinement by the hydrophobic layers force the expansion in the direction of the photonic crystal's layer periodicity, thus creating a material that is extremely and reversibly responsive to salt content. A unique interpretation of this employs volume change through cavity dissolution under solvent exposure. Rezaei *et al.* fabricated a lithography-free, cheap, single-use sensor from a metal-insulator-metal Fabry–Perot cavity made from porous nickel/PDMS/aluminum[198] (Fig. 21c). When immersed in solvent, the PDMS dissolves and diffuses through the porous Ni layer, resulting in shrinkage of the PDMS layer and a blue shift in the reflection spectrum. Rate of diffusion, dissolution, and therefore sensitivity is controlled by the crosslinker-monomer ratio in the PDMS layer. Careful choice of polymers and chemical moieties allows for targeted response to specific solvents or salt environments, allowing for solvent-responsive structural color.

3.1.4. pH-responsive structural color. pH-responsive structural colors change spacing or refractive index in response to pH changes, thereby providing a visual method of pH monitoring. pH response is enabled by the chemical structure of the materials used, often polymers with moieties that change volume when accepting or donating H^+, for example, carboxylic acids, pyridines, amides, or amines. This can cause volume changes and therefore color changes in photonic structures when incorporated. Xue *et al.* developed a pH-responsive inverse opal hydrogel film[199] from poly(acrylic acid) (PAA) capable of changing color from blue to red as pH increased from 2–7 (Fig. 22a). At pH $<$ 4, the carboxyl groups of PAA are protonated and the inverse opal pore spacing is like that of the template ($\sim$595 nm). As pH is increased, deprotonation of PAA causes the hydrogel to swell, increasing the spacing to 745 nm at pH 7 and shifting the color from blue to red. This swelling and color change is recoverable when the film is returned to a lower pH, with some noted hysteresis. When incorporated into a cellulose nanocrystal (CNC) system, pH and electrostatic repulsion can be used to control the spacing of the crystal. Through controlled oxidation, Yang *et al.* created CNCs of pitches between 145–270 nm corresponding to different colors and incorporated them into a plasticized film with colorimetric response to vapor pH[200] (Fig. 22b). When exposed to basic vapors, the CNCs are ionized, inducing electrostatic repulsion, and thereby increasing the pitch size and red shifting the color. Combining acrylic acids and amino groups, Liao *et al.* developed a multimodally responsive photonic crystal film from core–shell

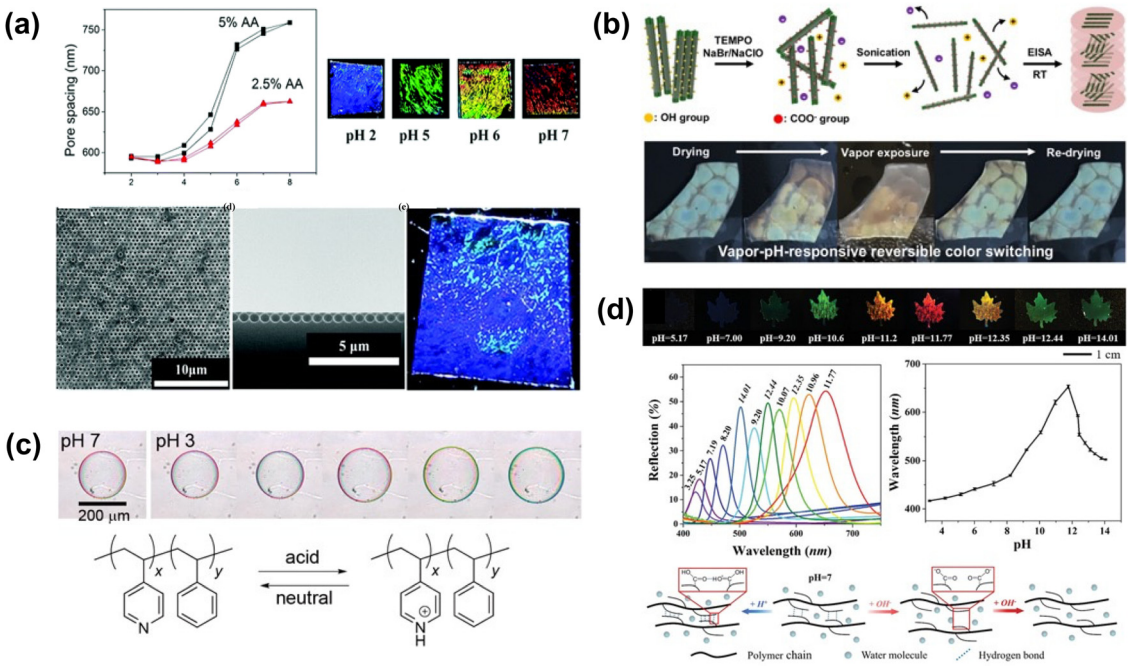

Fig. 22 (a) pH-dependent color change of the 2D inverse opal hydrogel *via* pH modulated pore spacing. [Reproduced from ref. 199, with permission from Royal Society of Chemistry, Copyright 2014]. (b) Schematic of the fabrication of oxidized CNC (OxCNC) films by evaporation-induced self-assembly. PEG/OxCNC composite film undergoes reversible color change upon vapor exposure. [Reproduced from ref. 200, with permission from Elsevier Publishing Group, Copyright 2019]. (c) Schematic illustration showing the mechanism of pH responsiveness for the films assembled by the copolymer nanoparticles. [Reproduced from ref. 202, with permission from American Chemical Society, Copyright 2016]. (d) Color and reflection spectra of the leaf pattern in response to solution with different pH value. [Reproduced from ref. 201, with permission from Wiley-VCH Verlag GmbH & Co. KGaA, Weinheim, Copyright 2019].

nanoparticles (NPs) coated in poly(acrylamide) (PAAm) and PAA.[201] The refractive index difference between the NP core and shell creates a periodic photonic crystal that generates color. Spacing between NP cores increases as the surface carboxyl and amino groups are deprotonated under increased pH, thereby inducing swelling and red shifting the observed color (Fig. 22d). A copolymer with protonatable pyridine moieties were used by Higashiguchi *et al.* in their structural color balloons,[202] submillimeter-sized capsules whose shells are thin enough to interfere with light and display structural color. The pyridine moiety can be protonated in the presence of paratoluene sulfonic acid (PTSA), upon which the polymer undergoes shrinkage, thereby decreasing the thickness of the shell and changing the color (Fig. 22c). There is a wide variety of well-established pH-responsive chemistry resulting in volume changes, all of which can be employed in unique ways to impart pH-responsive space tuning in structural color.

3.1.5. Photochromic structural colors. Light-responsive structural color occurs when certain wavelengths of light induce spatial changes in the color-generating structure. This can be combined with thermal transitions to induce a photothermal effect on a bulk scale; for example, absorption and conversion of near-infrared (NIR) light to heat can be used to thermally trigger volume changes in LCST polymers, thereby changing the spacing within the structure and therefore the color. This is usually done by incorporating a thermally conductive NIR absorber, such as carbon nanotubes (CNTs) or even candle soot. Xia *et al.* prepared a NIR-responsive structural color film by incorporating CNTs into a thermoresponsive poly(*N*-isopropyl acrylamide) (PNIPAAm) hydrogel containing core–shell microgel particles self-assembled into a 3D photonic crystal[203] (Fig. 23a). The CNTs absorb NIR radiation and convert it to heat, causing the hydrogel to shrink, thereby compressing the photonic crystal and blue-shifting the color. Xiong *et al.* also utilized the photothermal effect to imbue NIR solar light response to a thermoresponsive PNIPAAm inverse opal hydrogel.[204] A top layer of candle soot was used to improve NIR absorption and thermal conductivity (Fig. 23d). Under increased solar intensity, the photothermal effect induced shrinkage in the PNIPAAm and therefore shrinkage of the inverse opal. These conditions caused the reflection peak to shift from 640–460 nm, covering the visible light spectrum between red and blue. When combined with thermoresponsive polymers, the photothermal effect can be used to induce discrete spatial changes in structural color architectures.

On a molecular scale, dyes or chemical moieties that change shape under irradiation can be used to induce spatial changes in light-responsive structural color. The *cis–trans* isomerization of azobenzene is triggered upon changing between 365 and 450 nm light. Though the *trans*-isomer is 3.5 Å larger than the *cis*-isomer, *cis*-azobenzene occupies a larger volume as the phenyl rings are not coplanar.[208] Belmonte *et al.* incorporated

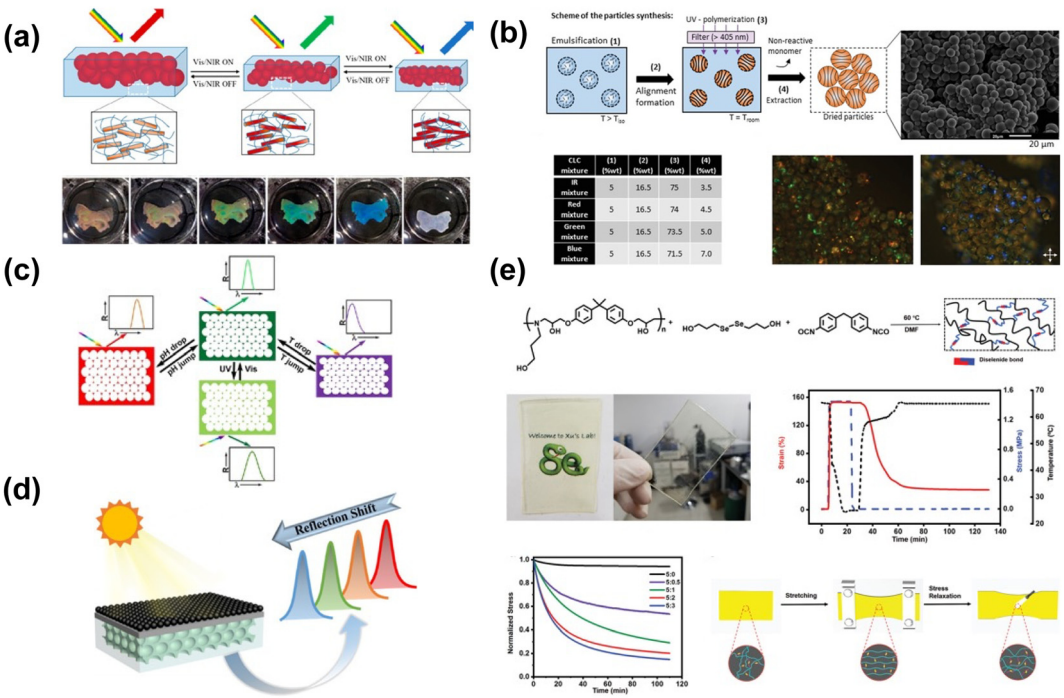

Fig. 23 (a) Scheme of the photonic hydrogel responsive to the NIR light with color and volume variation. [Reproduced from ref. 203, with permission from American Chemical Society, Copyright 2021]. (b) Scheme, SEM and polarized optical microscopy (POM) images of cholesteric liquid crystalline (CLC) polymer particles synthesis with various CLC monomer mixing formula. [Reproduced from ref. 205, with permission from Wiley-VCH Verlag GmbH & Co. KGaA, Weinheim, Copyright 2020]. (c) Model of environmental stimuli (temperature, pH or light) induced longitudinal swelling of the inverse opal hydrogel sensor. [Reproduced from ref. 206, with permission from Elsevier Publishing Group, Copyright 2018]. (d) Power-free and self-cleaning solar light detector based on the temperature-sensitive structural color and photothermal effect. [204]. (e) Diselenide-containing shape memory material and the controlled stress relaxation. [Reproduced from ref. 207, with permission from Wiley-VCH Verlag GmbH & Co. KGaA, Weinheim, Copyright 2020].

an azobenzene dye into particles of crosslinked chiral nematic cholesteric liquid crystal (CLC) copolymer[205] (Fig. 23b). The particles contain cholesteric layers arranged in a parallel, asymmetric configuration; interaction of light with these layers yields visible color. *Cis–trans* isomerization causes spatial changes in the CLC helical direction; elongation long the helical axis causes the color to red-shift. These particles exhibit spot- and arc-like reflective color from red to blue, and are independently light- and temperature responsive. Similarly, Zhao *et al.* imbued UV response to a temperature- and pH-responsive inverse opal structural color hydrogel by incorporating UV-responsive spiropyran into the copolymer.[206] Exposure to UV light causes the hydrogel's reflection peak to broaden and red-shift due to spatial changes affecting the hydrogel's refractive index caused by the spiropyran's response to UV light (Fig. 23c). In its native form, spiropyrans consist of heterocyclic functional groups in orthogonal planes. Under UV exposure, one of the heterocycles breaks, thereby changing the volume occupied by the molecule. One unique strategy to create light-responsive structural color films uses diselenide metathesis and shape memory properties. By applying strain, Liu *et al.* induced birefringent transmissive structural color in a film cast from a diselenide bond-containing shape memory polymer[207] (Fig. 23e). The films show a strong yellow color under polarized light. The diselenide bond is broken under visible light irradiation, thus releasing strain and eliminating the color. By masking certain areas of the film, it is possible to create an image, thus showing potential applications in counterfeit protection. Light-responsive chemical moieties are a powerful tool that can induce spatial changes in a bulk material, thereby allowing for multimodally responsive structural color.

3.1.6. Electrochromic structural colors. Electrically responsive structural colors change color under applied voltage, but the mechanism of electrical response can take many forms. The electrothermal effect can be used to induce volume changes in thermoresponsive polymers, while water splitting can be used to swell or de-swell hydrogels. Certain oxides, such as those from tungsten or nickel, undergo refractive index changes when incorporated into an electrochemical system through ion adsorption. The variety of mechanisms to induce volume or refractive index changes under applied voltage allows for diversity in realizing electrochromic structural color.

Electrochromic volume changes in polymers are often realized through a combination of responses, *e.g.* thermal or swelling responses. Park *et al.* used water splitting under 4V bias to impart deswelling in an inverse opal photonic gel fabricated from a charged polymer on a transparent electrode.[209] Under deswelling, the color changed from red to green as the photonic crystal structure was compressed (Fig. 24a). Froyen *et al.* employed an electrothermal effect to create electrically-responsive structural color,[210] using a thermally conductive silver nanowire substrate to heat a cholesteric liquid crystal (CLC) ink deposited on top (Fig. 24b). Increasing the applied voltage increases the heat and blue-shifts the observed color, going from colorless to red to green to blue as the liquid crystal

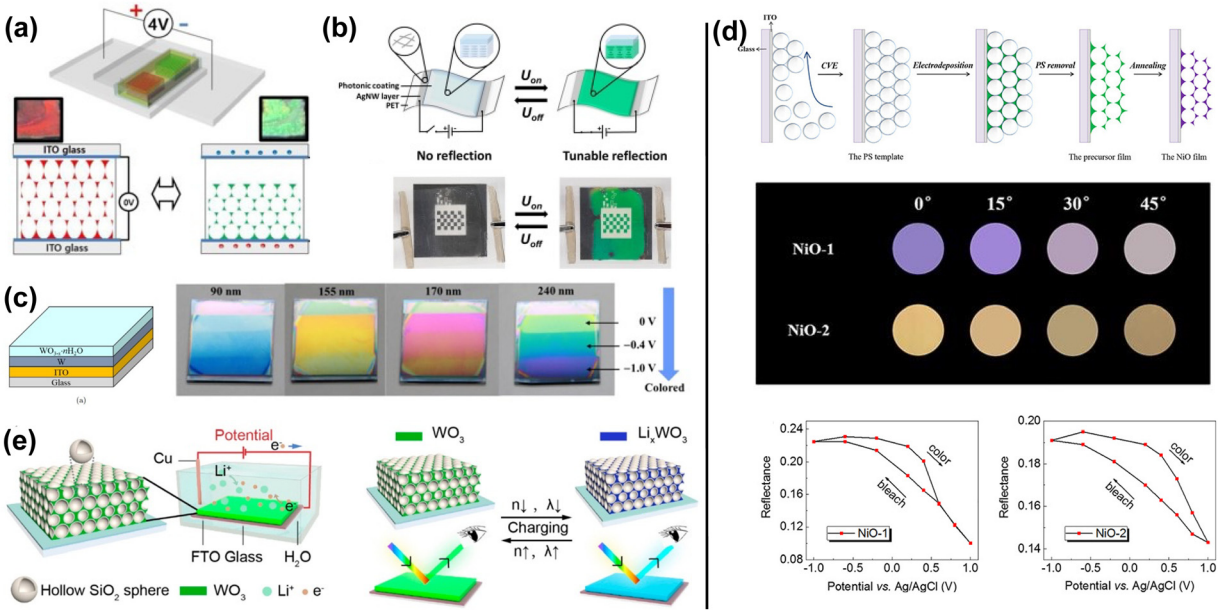

Fig. 24 (a) Schematic illustration of the longitudinal deswelling of inverse opal photonic gel with voltage bias from the fully swollen state. [Reproduced from ref. 209, with permission from Elsevier Publishing Group, Copyright 2020]. (b) Schematic representation of the electrochromic structural colored foil. A flexible, transparent silver nanowire/poly(ethylene terephthalate) (AgNW/PET) heater induces reflection band shifting under electrical stimulation. [Reproduced from ref. 210, with permission from American Chemical Society, Copyright 2022]. (c) Different color states (applied voltages of 0 V, −0.4 V and −1 V respectively) of four electrochromic films with various tungsten oxide thicknesses containing the colors of blue, yellow, pink and green. [Reproduced from ref. 211, with permission from World Scientific, Copyright 2021]. (d) Schematic diagram of the preparation of inverse opal NiO films. Reflectance of photonic band gap peaks at different potentials of two different NiO films is shown. [Reproduced from ref. 212, with permission from American Physical Society, Copyright 2021]. (e) Schematic demonstration of WO_3 PhC under electrochromic on–off states. [Reproduced from ref. 213, with permission from American Chemical Society, Copyright 2023].

transition is triggered. By using voltage to trigger volume change through thermal or swelling mechanisms, significant color change can be observed in electroresponsive structural color materials.

3.2. Artificial optical properties *via* refractive index tuning

3.2.1. Electrochromic materials. For materials that cannot undergo significant volume changes, such as oxides, refractive index control is used to modulate the observed color. Tungsten oxide (WO_3) or nickel oxide (NiO) are commonly used electrochromic oxides due to their reversibly adjustable optical constants and adjustable reflection peak in the visible light regime. Zhang *et al.* prepared an asymmetric Fabry–Perot resonator using sol–gel fabricated WO_3 as the dielectric cavity atop a metallic tungsten reflector,[211] which was then used as an electrochromic electrode in a Li^+-containing gel electrolyte system. Under applied voltage, Li^+ is inserted into the WO_3 layer, changing the refractive index and causing the color to shift from yellow to green between 0 and −1 V (Fig. 24c). Electrochromic oxides can also be employed in photonic crystal structures and have found use as an adjustable-index material in opals. Qu *et al.* fabricated a colored inverse opal structure[212] from electrochemically-deposited NiO (Fig. 24d) whose saturation can be varied by introducing an external potential in an LiCl electrolyte, again through absorption of Li^+. Similarly, Ran *et al.* designed an opal structure of hollow SiO_2 supported by WO_3.[213] Since an opal structure's color is determined by lattice parameter and refractive index, incorporation of index-tunable WO_3 allows for electroresponsive color change (Fig. 24e). Under applied voltage and in the presence of Li^+, the resulting film's reflection peaks could shift by 30–90 nm with obvious color change, allowing for a voltage-driven writing/erasing process with potential applications in display technology. Electroresponsive oxides are unique in that they are not polymer materials but capable of stimuli-responsive structural color through changes in refractive index rather than volume, demonstrating the diversity in strategies towards realizing electroresponsive structural color.

3.2.2. Dye-doped dielectrics. The incorporation of lossy inorganic dielectrics has been investigated in the past for structural color generation.[214–221] Due to the non-negligible imaginary part of the RI, an ultra-thin dielectric layer is good enough to produce decent coloration and angle-independent color[41,170,222–224] due to the relatively high real part of the refractive index. Modification of the absorber layer refractive index could also be achieved with careful design of a combination of two ultra-thin dielectrics as a meta-layer;[225,226] however, fine-tuning the spectrum of an optically thick dielectric layer is very challenging due to limitations from conventional deposition methods and the intrinsic broad absorption band of the dielectric material. Compared to lossy inorganics, organic dyes usually show a much narrower absorption band, which allows local fine-tuning of the absorptive property within a specific spectrum range (*i.e.* within the dye absorption range). Besides, as a small molecule, its solubility in various solvents could be easily determined by proper chemical modification.

We chose three dye molecules—rhodamine 6G (R6G), brilliant green (BG), and methylene blue (MB)—due to their good solubility in both water and ethanol as well as their compatibility with the dielectric precursors tetraethyl orthosilicate (TEOS) and titanium(IV) tetraisopropoxide (TTIP). As shown in Fig. 25a, the three dyes show a narrow absorption peak with ~100–150 nm bandwidth at three different wavelengths. Hence, local modification of the refractive index becomes possible with a dye-doped dielectric layer (dD). The dD layer can be deposited using a typical dip-coating method. Herein, we chose TiO_2 as the matrix material since it has a different real part of the refractive index than that of the dye.[227] Fig. 25b gives the experimentally determined refractive index of the coated dD layer from 1 wt% dye dissolved in the TiO_2 precursor solution. A quick comparison between the dyes' absorption spectra peaks and the imaginary part k of the coated dielectric reveals that the absorptive features of dyes have been integrated into the dielectric refractive index (Fig. 25b and c). The real part of the refractive index n also shows a distinctive anomalous dispersion feature due to the Kramers–Kronig relation[228] (K–K relation) between n and k. Further combination of the dye molecules leads to more complex refractive index behavior (Fig. 25d and e), where the refractive index starts to oscillate across the spectrum due to the absorption of dyes at different wavelengths. The magnitude of the imaginary part of the RI can also be tuned by the dye concentration in the precursor solution. A continuous change of the imaginary refractive index has been shown in Fig. 25d with increasing R6G concentration.

TiO_2 precursor solution with 1 wt% R6G or MB was dip-coated onto a silver layer coated substrate followed by another 15 nm silver layer deposited on top of the TiO_2 layer, resulting in a typical metal–dD–metal (M–dD–M) structure. Silver is chosen as both the top and bottom metal layer to maximize the lightness due to its low optical loss, and absorption in the structure is primarily governed by the dyes doped in the dielectric layer. Compared to undoped dip-coated TiO_2 samples, the samples doped with either R6G or BG/MB show much lower reflectivity when cavity resonance wavelength matches the dye-absorbing wavelength (Fig. 26a–c), giving a high contrast in the reflection spectra. The off-resonance wavelengths are only slightly affected as the dielectric layer is almost lossless in those wavelength regions. Hence, the overall reduction of lightness is mitigated compared to the un-doped samples because the absorptive property is only introduced near the resonance wavelength. Moreover, as the dyes boost their absorption efficiency inside the resonance cavity, the color chromaticity has been greatly improved as well (Fig. 26d–f). We can therefore expect that, with minimum amount of dye molecules inside the cavity, such an approach could benefit the coloring industry with its the environmental impact by reducing the use of dyes.[229]

3.2.3. Ultralow index dielectrics. Structural color from multilayered stacks (Bragg stacks or F–P cavities) often show color iridescence, *i.e.* the color changes with viewing angle. A closer look at the Bragg's law[230,231] indicates stronger angle dependency on the resonance wavelength when the refractive index of the cavity medium is lower. To push the dielectric refractive index to the limit, an aerogel film is adopted, which

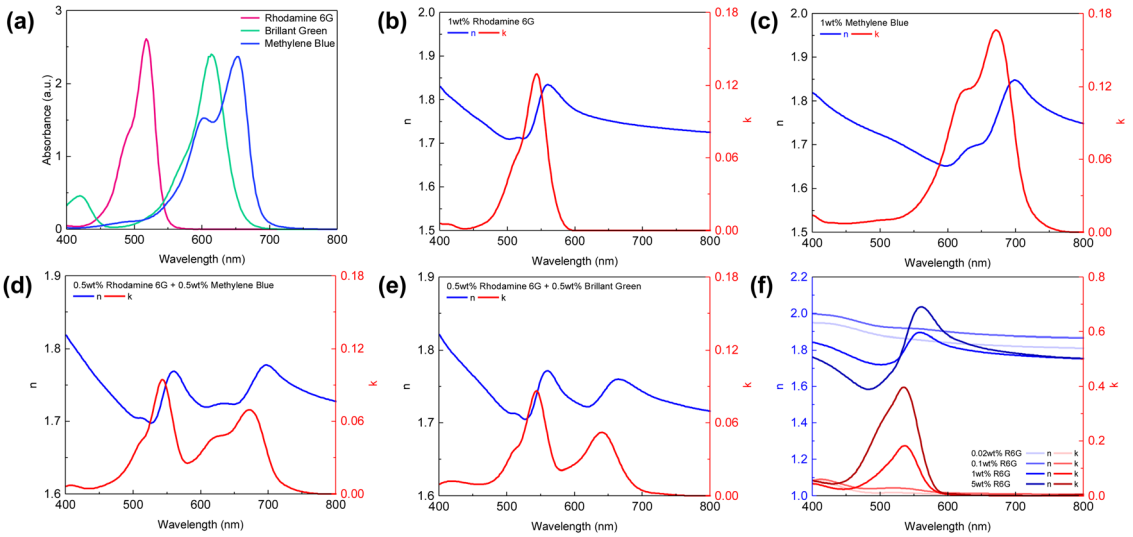

Fig. 25 (a) UV-Vis absorption spectra of rhodamine 6G (R6G), brilliant green (BG) and methylene blue (MB). (b)–(e) Extracted refractive index of dye-doped TiO_2, with 1 wt% total dye content dissolved in the precursor solution: (b) R6G, (c) MB, (d) BG + MB, and (e) R6G + BG. (f) Refractive index of R6G doped TiO_2 layer, with R6G concentration varying from 0.02 wt% to 5 wt% in the precursor solution.

possesses a refractive index barely above 1, making it an ideal candidate for super-iridescent structural color fabrication. Aerogel, as the name indicates, is a highly porous structure with most of the space filled with air. The air volume occupancy is typically around 95%–99% but could go even higher to 99.98%.

For the first time, we introduce SiO_2 aerogel as an ultra-low refractive index dielectric to the F–P cavity and demonstrate its super-iridescent color performance. The preparation of SiO_2 aerogel follows the logic of sol–gel chemistry[232–235] and uses a weak base (*i.e.* ammonia) to catalyze the condensation reactions. The TEOS molecules form small SiO_2 nanoparticles, and further undergo agglomeration once the nanoparticles reach a critical size. As more SiO_2 nanoparticles join, a SiO_2 framework forms and transforms the precursor solution into a porous gel. For the air void to form without collapsing the framework,[236] we incorporated a volatile solvent (*e.g.* hexane) to enhance the

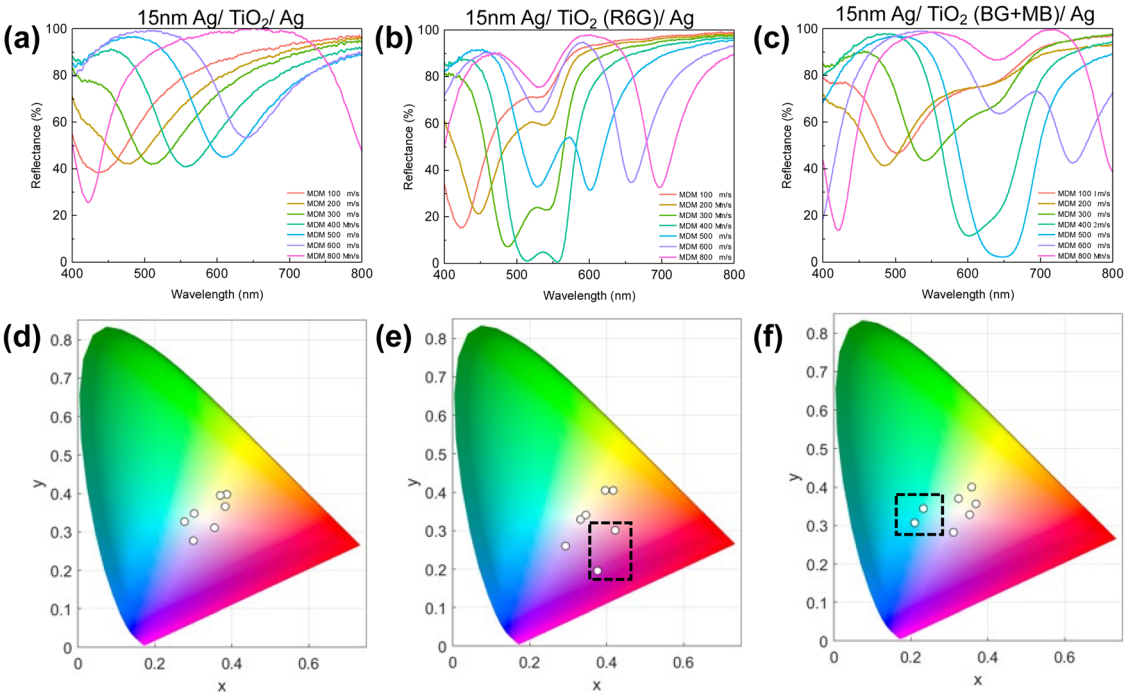

Fig. 26 (a) Reflection spectra of 15 nm Ag/TiO_2/Ag with TiO_2 being dip-coated on the Ag substrate. Reflection spectra of 15 nm Ag/TiO_2/Ag with TiO_2 dip-coated from (b) 1 wt% R6G and (c) 1 wt% MB + BG precursor solution. (d)–(f) Resulted coordinates in CIE color space correspond to the spectra in (a)–(c) respectively.

rate of solvent removal during spin-coating. SiO_2 aerogels with different refractive indexes are prepared with different TEOS concentrations. The resulting refractive index varies from 1.07 to 1.23 (Fig. 27a) with the increasing amount of TEOS being added. The low refractive index variation can be attributed to the porosity difference within the sample (Fig. 27b). The obtained tri-layer MDM structural color consists of 15nm Al/SiO_2 aerogel/Si and shows a very iridescent color (Fig. 27c) upon angle variation. Reflection spectra have been measured from oblique incident angles from 0° to 60° with 15° interval. As shown in Fig. 27d, significant blue shifts in the resonance wavelength were observed under increased viewing angle from normal. A change in the visual appearance is more drastic with the lowest refractive index (n = 1.07) aerogel, where color travels almost a closed trajectory on the CIE color space (Fig. 27e) upon angle variation. Such color iridescence is staggering where all three secondary colors (cyan, magenta, yellow) are reached within 60° angle variation. The possibility of substituting the air void with other medium like ethanol or toluene has also been explored where a high-order resonance can be obtained along with a dramatic color change (Fig. 27f). The entire process is fully reversible with the removal of solvent and thus provides new insight into designing solvent/vapor-based colorimetric sensors.

3.2.4. Effective medium. As described in 2.4.1, immobilization of plasmonic nanoparticles gives unique colors compared to bulk thin metal films. We showed that gold nanoparticle deposition density can be controlled by immersion time in nanoparticle solution. As observed in Fig. 28a, the surface coverage of nanoparticles increases with extended deposition time and finally plateaus after 6 hours. Fig. 28b reveals an increase in the imaginary part of the refractive index of the nanoparticle layer with increasing nanoparticle density. One could argue from the SEM image (Fig. 28a) that the gold nanoparticles along with its surrounding air matrix forms an effective composite layer. A further growth of the nanoparticle seed layer with $HAuCl_4$ and NH_2OH (as described at the end of 2.4.1) changes the fill fraction of the metal particles and hence the effective refractive index. Compared to the refractive index of the pristine gold nanoparticle layer (Fig. 28b), we notice an increase in both the real and imaginary part of the refractive index (Fig. 28c) in the longer wavelength regime (>500 nm), owing to the growth of the gold domains resembling the optical property of bulk gold.

A three-layer particle/dielectric/metal structure with various dielectric layer thicknesses were fabricated from dip-coating of SiO_2 on Si substrate followed by gold nanoparticle immobilization. Prominent reflection peaks appear (Fig. 29a) when the SiO_2 layer is thick (>100 nm), while interestingly, a broadband absorber is seen when the layer is thin (<80 nm), matching with the transfer-matrix method (TMM) simulation (Fig. 29b) using the effective refractive index of the gold nanoparticle layer. Various colors are therefore produced (Fig. 29c). Mao *et al.*[163] has provided a detailed explanation of such spectrum behavior where the disordered nanoparticles serve as a broadband absorber and the absorptive decay rate is equally partitioned into each wavelength.[237] No resonance mode is built up when the dielectric layer is thin (*i.e.* broadband absorber), while in a thicker dielectric layer, a mismatch shows up between the absorption decay rates and the radiation decay rates at the

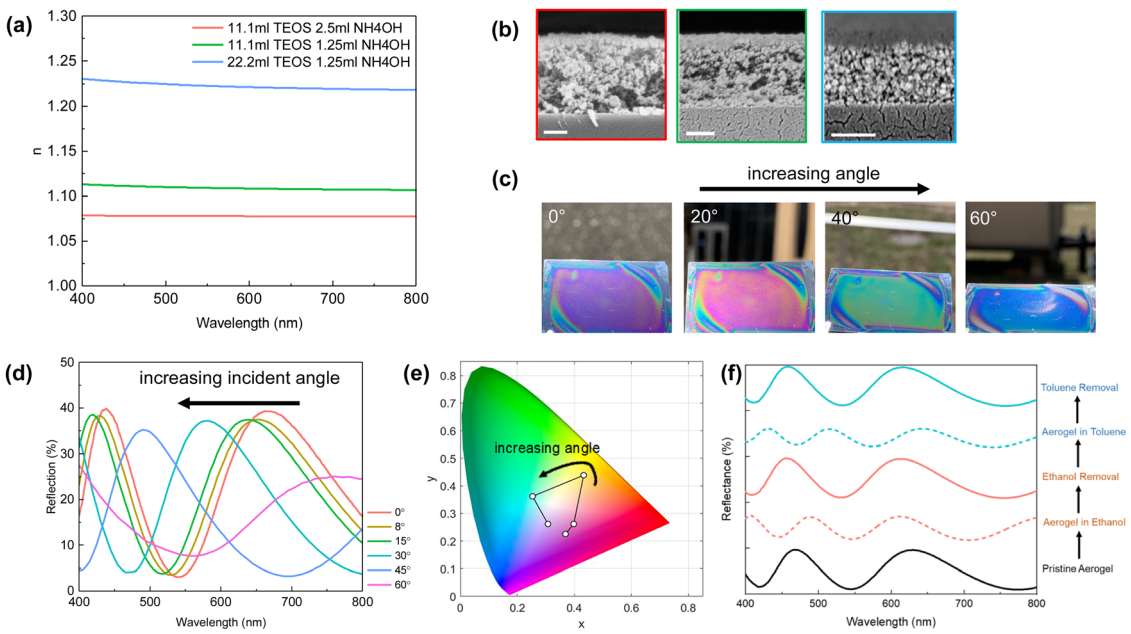

Fig. 27 (a) Spin-coated aerogels with different refractive indices by changing TEOS concentration. (b) Cross-section SEM image of aerogels with a refractive index of 1.07, 1.14 and 1.23 (from left to right). (c) Photos, (d) angle-resolved reflection spectra, and (e) corresponding CIE diagram of 15 nm Al/Aerogel (n = 1.07)/Si film at various angles showing a large color change. (f) Reflection spectra of 15 nm Al/Aerogel (n = 1.07)/Si immersed in solvents (*i.e.* ethanol and toluene) and upon solvent removal.

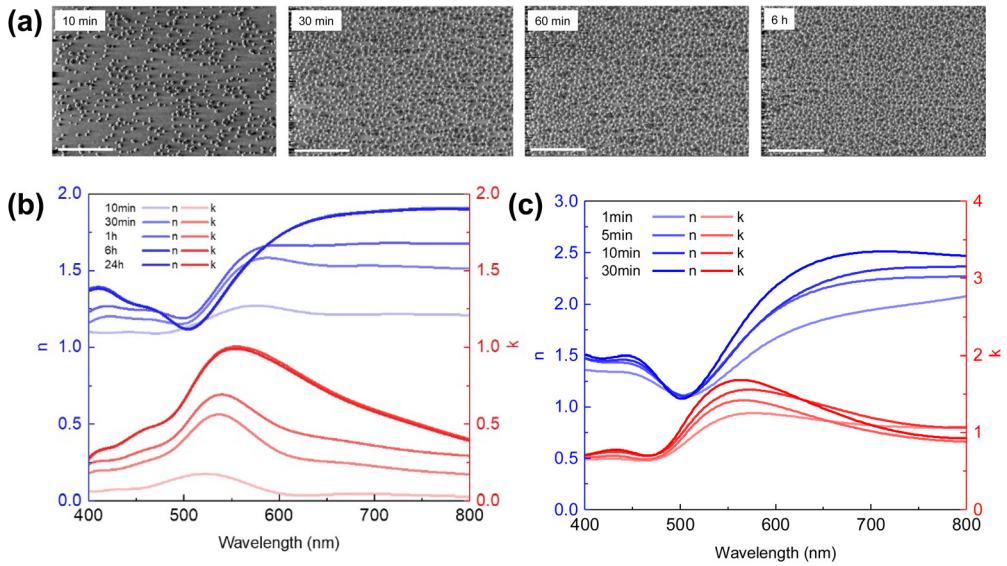

Fig. 28 (a) SEM image of direct deposition of as-synthesized 14 nm gold nanoparticles on APTES functionalized surface for 10 min, 30 min, 1 h, and 6 h and (b) corresponding refractive index. Scale bar: 500 nm. (c) Measured refractive index of the top gold nanoparticle layer with various growth time.

resonance wavelength, leading to a strong reflection peak. The non-continuous particulate metal layer thus enables new ways of tuning the optical property of broadband lossy dielectric across the visible spectrum.

4. Summary and future outlook

4.1. Merits of solution-processed structural color

Overall, solution-processed structural color offers a cost-effective, scalable, and flexible approach to generating color through nanoscale manipulation of light. The simplicity and cost-effectiveness of solution processing methods, such as self-assembly, dip-coating, spray coating, electrochemical and electrostatic-based deposition, enable large-scale production, making it economically viable for applications like displays and sensors. Many of these approaches also allow for easy integration with flexible substrates, facilitating the development of bendable and stretchable devices. Additionally, the potential for energy efficiency makes solution-processed structural color versatile in design and environmentally friendly. Table 1 presents a comparison of commonly employed methods for structural color coating. Each method offers a niche application regarding material choice, achievable film thickness and application scenarios.

Moreover, solution-processed structural colors stand out for their exceptional tunability in responding to external stimuli and altering optical properties, which would be challenging to achieve through vacuum-deposited materials. A range of solution-processable materials is employed to tune the size, refractive index, and spacing in producing the structural colors. Polymers undergoing volume changes in response to strain, temperature, or solvent swelling, at the bulk and macromolecular scale, can be integrated into photonic crystals or Fabry–Perot cavities, altering their spacing and resulting color. At the molecular and atomic scale, polymers and sol–gel oxides responsive to light, electricity, or pH can modulate their volume or refractive index, affecting the optical path length within incorporated photonic structures. Solution methods also facilitate the effortless mixing and formulation of material components, offering versatility in creating and modulating effective refractive index properties. The artificial synthesis of optical materials, in turn, imparts distinctive color perceptions, thereby enhancing the appeal for decorations, sensing, and anti-counterfeiting, amongst other applications.

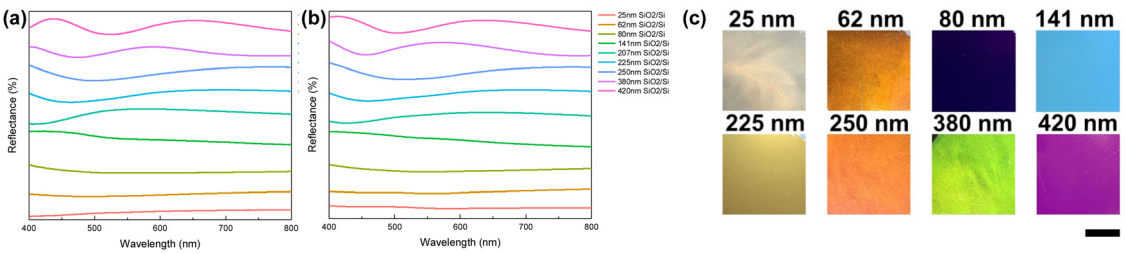

Fig. 29 (a) Experimentally measured and (b) TMM simulated reflection spectra of AuNP/SiO_2/Si with various SiO_2 thicknesses, and (c) their corresponding color appearance. Scale bar: 1 cm.

Table 1 A comparison of solution-based structural color fabrication methods

Methods	Material choice	Unit film thickness	Advantage	Disadvantage
Self-assembly	Polymers, colloids	$>10^3$ nm	Facile, scalable	Low-throughput, non-uniform
Layer-by-layer coating (LbL)	Polyelectrolytes	$\sim10^0$ nm	Conformal, precise thickness control	Very low-throughput
Dip coating	Polymers, particles, dielectrics	10^1–10^2 nm	Facile, scalable, no pre-syntheis	Edge effect, non-conformal
Spin coating	Polymers, particles, dielectrics	10^1–10^2 nm	Facile, rapid	Edge effect, non-conformal, non-scalable
Spray coating	Particles, polymers	$>10^2$ nm	Facile, rapid, scalable, conformal	Nozzle clogging
Electroless deposition (ELD)	Metals	$>10^0$ nm	Facile, rapid, scalable, conformal	Require fresh solution
Electrodeposition (ED)	Metals, dielectrics	$>10^0$ nm	Facile, rapid, scalable, conformal	Require conductive substrate, secondary reaction possible
Electrophoretic deposition (EPD)	Charged particles	Depend on particle size	Facile, conformal	Require conductive substrate large voltage and pre-synthesis

4.2. Future perspectives

Solution processes leverage solution chemistry to enable versatile and facile material and photonic structure design. Compared to mature vacuum-based deposition technology, solution-processed methods for fabricating structural color still encounter significant challenges before achieving commercial viability: (1) color uniformity over large area. Solution process, being a bottom-up fabrication method, faces limitations in achieving uniformity across the entire film. Molecules or nano-/micro-particles cannot perceive the global environment outside their entirety. This can result in non-uniformity or defects at the macro-scale, such as edge effects. Rigorous engineering control is essential to maintain a consistent micro-environment across the substrate. (2) Encapsulation. Structural color films produced through solution processing tend to be less compact and more fragile, making them prone to scratching and environmental damage. While their susceptibility to environmental changes makes them suitable for sensor applications, it also compromises color stability when consistent color perception is required. Therefore, applying a protective layer atop the colored film becomes crucial to prevent external molecule infiltration and mitigate scratching. Common strategies involve additional coating layers of materials like acrylic polymer or hard dielectrics such as ZrO_2 onto the colored structure. (3) Compatibility. Ensuring compatibility between each layer coating in terms of structure and recipe is paramount in solution-processed structures. Materials with different properties, such as metals and dielectrics, must not only adhere closely to each other without inducing excessive internal stress but also remain intact under various fabrication conditions. Further research efforts are necessary to develop reliable and compatible coating recipes for future advancements in this field. Hence, we emphasize the significance of future interdisciplinary research, with ample opportunity for collaboration between the chemistry, nanofabrication, materials science, and photonics communities.

Engineering novel optical materials through solution-based synthesis remains an emerging area of research. Similar to doping dye into dielectrics, active components like fluorescent molecules can also be doped into the dielectric and further incorporated into resonant cavities. Potential applications in the field of emissive devices, sensors and even lasers could be possible. On the other hand, solution-synthesized particles can have various shapes such as nanorods,[157,158,238,239] nanodisks[161,240,241] and even nanopolyhedrons[242,243] and components with absorption/resonance wavelength varying across the visible spectrum. A careful study and control on nanoparticle geometry, arrangements, order could further revolutionize the field of optical metasurface or metamaterial fabrication, where large scale production and cost-effective devices could be made possible.

Data availability

No primary research results, software or code have been included and no new data were generated or analyzed as part of this review.

Conflicts of interest

Certain aspects of the content presented in the manuscript is the subject of a US provisional patent application.

Acknowledgements

The authors would like to acknowledge the support by the National Science Foundation (PFI- 2213684).

References

1 J. Sun, B. Bhushan and J. Tong, Structural coloration in nature, *RSC Adv.*, 2013, **3**, 14862–14889.
2 S. Kinoshita, *Structural Colors in the Realm of Nature*, 2008, DOI: **10.1142/9789812709752_fmatter**.
3 G. S. Smith, Structural color of Morpho butterflies, *Am. J. Phys.*, 2009, **77**, 1010–1019.
4 S. Kinoshita, S. Yoshioka, Y. Fujii and N. Okamoto, Photophysics of Structural Color in the Morpho Butterflies, *Forma*, 2002, **17**, 103–121.
5 J. Zi, *et al.*, Coloration strategies in peacock feathers, *Proc. Natl. Acad. Sci. U. S. A.*, 2003, **100**, 12576.

6 A. E. Luna, D. C. Skigin, M. E. Inchaussandague and A. R. Alsina, Structural color in beetles of South America, in *The Nature of Light: Light in Nature III*, vol. 778205, 2010, DOI: 10.1117/12.858695.
7 H. Yin, *et al.*, Amorphous diamond-structured photonic crystal in the feather barbs of the scarlet macaw, *Proc. Natl. Acad. Sci. U. S. A.*, 2012, **109**, 10798–10801.
8 B. Datta, E. F. Spero, F. J. Martin-Martinez and C. Ortiz, Socially-Directed Development of Materials for Structural Color, *Adv. Mater.*, 2022, **34**, 2100939.
9 Y. Liu, *et al.*, Structural color three-dimensional printing by shrinking photonic crystals, *Nat. Commun.*, 2019, **10**, 4340.
10 X. Su, H. Xia, S. Zhang, B. Tang and S. Wu, Vivid structural colors with low angle dependence from long-range ordered photonic crystal films, *Nanoscale*, 2016, **9**, 3002–3009.
11 Y. Zhang, *et al.*, Using Cuttlefish Ink as an Additive to Produce-Non-iridescent Structural Colors of High Color Visibility, *Adv. Mater.*, 2015, **27**, 4719–4724.
12 V. L. Colvin, From Opals to Optics: Colloidal Photonic Crystals, *MRS Bull.*, 2001, **26**, 637–641.
13 D. Yan, *et al.*, Flexible construction of cellulose photonic crystal optical sensing nano-materials detecting organic solvents, *Analyst*, 2018, **144**, 1892–1897.
14 H. K. Raut, *et al.*, Hierarchical Colorful Structures by Three-Dimensional Printing of Inverse Opals, *Nano Lett.*, 2021, **21**, 8602–8608.
15 H. Galinski, *et al.*, Scalable, ultra-resistant structural colors based on network metamaterials, *Light: Sci. Appl.*, 2017, **6**, e16233.
16 L. Feng, P. Huo, Y. Liang and T. Xu, Photonic Metamaterial Absorbers: Morphology Engineering and Interdisciplinary Applications, *Adv. Mater.*, 2020, **32**, e1903787.
17 F. Cheng, *et al.*, Aluminum plasmonic metamaterials for structural color printing, *Opt. Express*, 2015, **23**, 14552–14560.
18 M. Song, *et al.*, Colors with plasmonic nanostructures: A full-spectrum review, *Appl. Phys. Rev.*, 2019, **6**, 041308.
19 J. Xue, *et al.*, Scalable, full-colour and controllable chromotropic plasmonic printing, *Nat. Commun.*, 2015, **6**, 8906.
20 H. Wang, *et al.*, Full Color Generation Using Silver Tandem Nanodisks, *ACS Nano*, 2017, **11**, 4419–4427.
21 T. Xu, Y.-K. Wu, X. Luo and L. J. Guo, Plasmonic nanoresonators for high-resolution colour filtering and spectral imaging, *Nat. Commun.*, 2010, **1**, 59.
22 A. E. Schlather, P. Gieri, M. Robinson, S. A. Centeno and A. Manjavacas, Nineteenth-century nanotechnology: The plasmonic properties of daguerreotypes, *Proc. Natl. Acad. Sci. U. S. A.*, 2019, **116**, 13791–13798.
23 A. Kristensen, *et al.*, Plasmonic colour generation, *Nat. Rev. Mater.*, 2016, **2**, 16088.
24 C. Yang, *et al.*, Compact Multilayer Film Structures for Ultrabroadband, Omnidirectional, and Efficient Absorption, *ACS Photonics*, 2016, **3**, 590–596.
25 K.-T. Lee, S. Y. Han, Z. Li, H. W. Baac and H. J. Park, Flexible High-Color-Purity Structural Color Filters Based on a Higher-Order Optical Resonance Suppression, *Sci. Rep.*, 2019, **9**, 14917.
26 B. A. Rorem, *et al.*, Integrating Structural Colors with Additive Manufacturing Using Atomic Layer Deposition, *ACS Appl. Mater. Interfaces*, 2022, **14**, 31099–31108.
27 X. Yuan, *et al.*, Properties and application of multifunctional and structurally colored textile prepared by magnetron sputtering, *J. Ind. Text.*, 2022, **51**, 1295–1311.
28 M. Huang, *et al.*, Structural coloration and its application to textiles: a review, *J. Text. Inst.*, 2020, **111**, 756–764.
29 F. Cheng, J. Gao, T. S. Luk and X. Yang, Structural color printing based on plasmonic metasurfaces of perfect light absorption, *Sci. Rep.*, 2015, **5**, 11045.
30 H. Wang, *et al.*, Full Color and Grayscale Painting with 3D Printed Low-Index Nanopillars, *Nano Lett.*, 2021, **21**, 4721–4729.
31 S. Sun, *et al.*, All-Dielectric Full-Color Printing with TiO2 Metasurfaces, *ACS Nano*, 2017, **11**, 4445–4452.
32 Y. Shen, *et al.*, Structural Colors from Fano Resonances, *ACS Photonics*, 2015, **2**, 27–32.
33 C. Zhang, *et al.*, Printed photonic elements: nanoimprinting and beyond, *J. Mater. Chem. C*, 2016, **4**, 5133–5153.
34 A. F. Kaplan, T. Xu and L. J. Guo, High efficiency resonance-based spectrum filters with tunable transmission bandwidth fabricated using nanoimprint lithography, *Appl. Phys. Lett.*, 2011, **99**, 143111.
35 Z. Li, *et al.*, High-Efficiency, Mass-Producible, and Colored Solar Photovoltaics Enabled by Self-Assembled Photonic Glass, *ACS Nano*, 2022, **16**, 11473–11482.
36 A. L. Liberman-Martin, C. K. Chu and R. H. Grubbs, Application of Bottlebrush Block Copolymers as Photonic Crystals, *Macromol. Rapid Commun.*, 2017, **38**, 1700058.
37 D.-P. Song, T. H. Zhao, G. Guidetti, S. Vignolini and R. M. Parker, Hierarchical Photonic Pigments via the Confined Self-Assembly of Bottlebrush Block Copolymers, *ACS Nano*, 2019, **13**, 1764–1771.
38 K. P. Velikov, A. Moroz and A. V. Blaaderen, Photonic crystals of core-shell colloidal particles, *Appl. Phys. Lett.*, 2002, **80**, 49–51.
39 E. S. A. Goerlitzer, R. N. K. Taylor and N. Vogel, Bioinspired Photonic Pigments from Colloidal Self-Assembly, *Adv. Mater.*, 2018, **30**, 1706654.
40 D. Wang, *et al.*, Structural color generation: from layered thin films to optical metasurfaces, *Nanophotonics*, 2023, **12**, 1019–1081.
41 K. Mao, *et al.*, Angle Insensitive Color Filters in Transmission Covering the Visible Region, *Sci. Rep.*, 2016, **6**, 19289.
42 C. Ji, *et al.*, Decorative near-infrared transmission filters featuring high-efficiency and angular-insensitivity employing 1D photonic crystals, *Nano Res.*, 2019, **12**, 543–548.
43 Z. Yang, C. Ji, Q. Cui and L. J. Guo, High-Purity Hybrid Structural Colors by Enhancing Optical Absorption of Organic Dyes in Resonant Cavity, *Adv. Opt. Mater.*, 2020, **8**, 2000317.
44 C. Yang, *et al.*, Compact Multilayer Film Structure for Angle Insensitive Color Filtering, *Sci. Rep.*, 2015, **5**, 9285.
45 N. S. King, *et al.*, Fano Resonant Aluminum Nanoclusters for Plasmonic Colorimetric Sensing, *ACS Nano*, 2015, **9**, 10628.

46 A. E. Goodling, *et al.*, Colouration by total internal reflection and interference at microscale concave interfaces, *Nature*, 2019, **566**, 523–527.
47 S. D. Abdurakhmonov, M. S. Ashurov, S. O. Klimonsky and N. V. Tcherniega, Numerical Simulation of Optical Properties of Photonic Crystals with Inverse Opal Structure, *Bull. Lebedev Phys. Inst.*, 2022, **49**, 137–144.
48 C. D. Dushkin, K. Nagayama, T. Miwa and P. A. Kralchevsky, Colored multilayers from transparent submicrometer spheres, *Langmuir*, 1993, **9**, 3695–3701.
49 S. John, Strong localization of photons in certain disordered dielectric superlattices, *Phys. Rev. Lett.*, 1987, **58**, 2486–2489.
50 E. Yablonovitch, Inhibited Spontaneous Emission in Solid-State Physics and Electronics, *Phys. Rev. Lett.*, 1987, **58**, 2059–2062.
51 S. A. Asher, J. Holtz, L. Liu and Z. Wu, Self-Assembly Motif for Creating Submicron Periodic Materials. Polymerized Crystalline Colloidal Arrays, *J. Am. Chem. Soc.*, 1994, **116**, 4997–4998.
52 P. Jiang, J. F. Bertone, K. S. Hwang and V. L. Colvin, Single-Crystal Colloidal Multilayers of Controlled Thickness, *Chem. Mater.*, 1999, **11**, 2132–2140.
53 B. Frka-Petesic, G. Guidetti, G. Kamita and S. Vignolini, Controlling the Photonic Properties of Cholesteric Cellulose Nanocrystal Films with Magnets, *Adv. Mater.*, 2017, **29**, 1701469.
54 T. Ding, K. Song, K. Clays and C. Tung, Fabrication of 3D Photonic Crystals of Ellipsoids: Convective Self-Assembly in Magnetic Field, *Adv. Mater.*, 2009, **21**, 1936–1940.
55 H. Wang, K. P. Yan, J. Xie and M. Duan, Fabrication of ZnO colloidal photonic crystal by spin-coating method, *Mater. Sci. Semicond. Process.*, 2008, **11**, 44–47.
56 R. Pozas, A. Mihi, M. Ocaña and H. Míguez, Building Nanocrystalline Planar Defects within Self-Assembled Photonic Crystals by Spin-Coating, *Adv. Mater.*, 2006, **18**, 1183–1187.
57 W. Yuan, N. Zhou, L. Shi and K.-Q. Zhang, Structural Coloration of Colloidal Fiber by Photonic Band Gap and Resonant Mie Scattering, *ACS Appl. Mater. Interfaces*, 2015, **7**, 14064–14071.
58 H. Nakamura, M. Ishii, A. Tsukigase, M. Harada and H. Nakano, Close-Packed Colloidal Crystalline Arrays Composed of Silica Spheres Coated with Titania, *Langmuir*, 2006, **22**, 1268–1272.
59 M. Xiao, *et al.*, Bio-Inspired Structural Colors Produced via Self-Assembly of Synthetic Melanin Nanoparticles, *ACS Nano*, 2015, **9**, 5454–5460.
60 J. E. G. J. Wijnhoven and W. L. Vos, Preparation of Photonic Crystals Made of Air Spheres in Titania, *Science*, 1998, **281**, 802–804.
61 G. I. N. Waterhouse, W.-T. Chen, A. Chan and D. Sun-Waterhouse, Achieving Color and Function with Structure: Optical and Catalytic Support Properties of ZrO2 Inverse Opal Thin Films, *ACS Omega*, 2018, **3**, 9658–9674.
62 J. E. S. Hoeven, A. V. van der, Shneidman, N. J. Nicolas and J. Aizenberg, Evaporation-Induced Self-Assembly of Metal Oxide Inverse Opals: From Synthesis to Applications, *Acc. Chem. Res.*, 2022, **55**, 1809–1820.
63 F. Liu, B. Shan, S. Zhang and B. Tang, SnO2 Inverse Opal Composite Film with Low-Angle-Dependent Structural Color and Enhanced Mechanical Strength, *Langmuir*, 2018, **34**, 3918–3924.
64 P. Liu, *et al.*, Self-assembled colloidal arrays for structural color, *Nanoscale Adv.*, 2019, **1**, 1672–1685.
65 Y. Takeoka, M. Honda, T. Seki, M. Ishii and H. Nakamura, Structural Colored Liquid Membrane without Angle Dependence, *ACS Appl. Mater. Interfaces*, 2009, **1**, 982–986.
66 K. Ueno, A. Inaba, Y. Sano, M. Kondoh and M. Watanabe, A soft glassy colloidal array in ionic liquid, which exhibits homogeneous, non-brilliant and angle-independent structural colours, *Chem. Commun.*, 2009, 3603–3605.
67 R. O. Prum, R. H. Torres, S. Williamson and J. Dyck, Coherent light scattering by blue feather barbs, *Nature*, 1998, **396**, 28–29.
68 R. O. Prum, E. R. Dufresne, T. Quinn and K. Waters, Development of colour-producing -keratin nanostructures in avian feather barbs, *J. R. Soc., Interface*, 2009, **6**, S253–S265.
69 L. Shi, *et al.*, Macroporous oxide structures with short-range order and bright structural coloration: a replication from parrot feather barbs, *J. Mater. Chem.*, 2009, **20**, 90–93.
70 Y. Zhang, B. Dong, X. Liu and J. Zi, Replication of spinodally decomposed structures with structural coloration from scales of the longhorn beetle Sphingnotus mirabilis, *Bioinspiration Biomimetics*, 2013, **8**, 045003.
71 A. Farhadi, T. Bartschmid and G. R. Bourret, Dewetting-Assisted Patterning: A Lithography-Free Route to Synthesize Black and Colored Silicon, *ACS Appl. Mater. Interfaces*, 2023, **15**, 44087–44096.
72 P. Liu, *et al.*, Bio-inspired robust non-iridescent structural color with self-adhesive amorphous colloidal particle arrays, *Nanoscale*, 2017, **10**, 3673–3679.
73 G. H. Lee, J. B. Kim, T. M. Choi, J. M. Lee and S. Kim, Structural Coloration with Nonclose-Packed Array of Bidisperse Colloidal Particles, *Small*, 2019, **15**, e1804548.
74 T. Liu, B. VanSaders, S. C. Glotzer and M. J. Solomon, Effect of Defective Microstructure and Film Thickness on the Reflective Structural Color of Self-Assembled Colloidal Crystals, *ACS Appl. Mater. Interfaces*, 2020, **12**, 9842–9850.
75 T. Liu, B. VanSaders, J. T. Keating, S. C. Glotzer and M. J. Solomon, Effect of Particles of Irregular Size on the Microstructure and Structural Color of Self-Assembled Colloidal Crystals, *Langmuir*, 2021, **37**, 13300–13308.
76 P. P. Lele and E. M. Furst, Assemble-and-Stretch Method for Creating Two- and Three-Dimensional Structures of Anisotropic Particles, *Langmuir*, 2009, **25**, 8875–8878.
77 T. Liu, T. Liu, F. Gao, S. C. Glotzer and M. J. Solomon, Structural Color Spectral Response of Dense Structures of Discoidal Particles Generated by Evaporative Assembly, *J. Phys. Chem. B*, 2022, **126**, 1315–1324.
78 S. Vignolini, *et al.*, Pointillist structural color in Pollia fruit, *Proc. Natl. Acad. Sci. U. S. A.*, 2012, **109**, 15712–15715.

79 S. N. Fernandes, *et al.*, Structural Color and Iridescence in Transparent Sheared Cellulosic Films, *Macromol. Chem. Phys.*, 2013, **214**, 25–32.
80 B. G. Rånby, A. Banderet and L. G. Sillén, Aqueous Colloidal Solutions of Cellulose Micelles, *Acta Chem. Scand.*, 1949, **3**, 649–650.
81 K. Conley, L. Godbout, M. T. Whitehead and T. G. van de Ven, Origin of the twist of cellulosic materials, *Carbohydr. Polym.*, 2016, **135**, 285–299.
82 J. Pan, W. Hamad and S. K. Straus, Parameters Affecting the Chiral Nematic Phase of Nanocrystalline Cellulose Films, *Macromolecules*, 2010, **43**, 3851–3858.
83 J. P. F. Lagerwall, *et al.*, Cellulose nanocrystal-based materials: from liquid crystal self-assembly and glass formation to multifunctional thin films, *NPG Asia Mater.*, 2014, **6**, e80.
84 B. Frka-Petesic, G. Guidetti, G. Kamita and S. Vignolini, Controlling the Photonic Properties of Cholesteric Cellulose Nanocrystal Films with Magnets, *Adv. Mater.*, 2017, **29**, 1701469.
85 J. Araki and S. Kuga, Effect of Trace Electrolyte on Liquid Crystal Type of Cellulose Microcrystals, *Langmuir*, 2001, **17**, 4493–4496.
86 P.-X. Wang, W. Y. Hamad and M. J. MacLachlan, Structure and transformation of tactoids in cellulose nanocrystal suspensions, *Nat. Commun.*, 2016, **7**, 11515.
87 X. Mu and D. G. Gray, Formation of Chiral Nematic Films from Cellulose Nanocrystal Suspensions Is a Two-Stage Process, *Langmuir*, 2014, **30**, 9256–9260.
88 A. G. Dumanli, *et al.*, Controlled, Bio-inspired Self-Assembly of Cellulose-Based Chiral Reflectors, *Adv. Opt. Mater.*, 2014, **2**, 646–650.
89 T. G. Parton, *et al.*, Chiral self-assembly of cellulose nanocrystals is driven by crystallite bundles, *Nat. Commun.*, 2022, **13**, 2657.
90 G. Kamita, *et al.*, Biocompatible and Sustainable Optical Strain Sensors for Large-Area Applications, *Adv. Opt. Mater.*, 2016, **4**, 1950–1954.
91 C. E. Boott, A. Tran, W. Y. Hamad and M. J. MacLachlan, Cellulose Nanocrystal Elastomers with Reversible Visible Color, *Angew. Chem., Int. Ed.*, 2020, **59**, 226–231.
92 K. Adstedt, *et al.*, Chiral Cellulose Nanocrystals with Intercalated Amorphous Polysaccharides for Controlled Iridescence and Enhanced Mechanics, *Adv. Funct. Mater.*, 2020, **30**, 2003597.
93 J. Wang, Q. Cheng, L. Lin and L. Jiang, Synergistic Toughening of Bioinspired Poly(vinyl alcohol)–Clay–Nanofibrillar Cellulose Artificial Nacre, *ACS Nano*, 2014, **8**, 2739–2745.
94 S. Beck, J. Bouchard and R. Berry, Controlling the Reflection Wavelength of Iridescent Solid Films of Nanocrystalline Cellulose, *Biomacromolecules*, 2011, **12**, 167–172.
95 K. E. Shopsowitz, W. Y. Hamad and M. J. MacLachlan, Flexible and Iridescent Chiral Nematic Mesoporous Organosilica Films, *J. Am. Chem. Soc.*, 2012, **134**, 867–870.
96 K. E. Shopsowitz, H. Qi, W. Y. Hamad and M. J. MacLachlan, Free-standing mesoporous silica films with tunable chiral nematic structures, *Nature*, 2010, **468**, 422–425.
97 B. E. Droguet, *et al.*, Large-scale fabrication of structurally coloured cellulose nanocrystal films and effect pigments, *Nat. Mater.*, 2022, **21**, 352–358.
98 T. Heinze, Cellulose Chemistry and Properties: Fibers, Nanocelluloses and Advanced Materials, *Adv. Polym. Sci.*, 2015, 1–52, DOI: 10.1007/12_2015_319.
99 M. H. Godinho, D. G. Gray and P. Pieranski, Revisiting (hydroxypropyl) cellulose (HPC)/water liquid crystalline system, *Liq. Cryst.*, 2017, 1–13, DOI: 10.1080/02678292.2017.1325018.
100 R. S. Werbowyj and D. G. Gray, Liquid Crystalline Structure In Aqueous Hydroxypropyl Cellulose Solutions, *Mol. Cryst. Liq. Cryst.*, 1976, **34**, 97–103.
101 H. Shimokawa, K. Hayata, M. Fukawa and S. Furumi, Fabrication of Reflective Color Films from Cellulose Derivatives, *J. Photopolym. Sci. Technol.*, 2020, **33**, 467–471.
102 R. S. Werbowyj and D. G. Gray, Optical properties of hydroxypropyl cellulose liquid crystals. I. Cholesteric pitch and polymer concentration, *Macromolecules*, 1984, **17**, 1512–1520.
103 C. H. Barty-King, *et al.*, Mechanochromic, Structurally Colored, and Edible Hydrogels Prepared from Hydroxypropyl Cellulose and Gelatin, *Adv. Mater.*, 2021, **33**, 2102112.
104 H.-L. Liang, *et al.*, Roll-to-roll fabrication of touch-responsive cellulose photonic laminates, *Nat. Commun.*, 2018, **9**, 4632.
105 Y.-S. Yang, Y. Zhou, F. B. Y. Chiang and Y. Long, Temperature-responsive hydroxypropylcellulose based thermochromic material and its smart window application, *RSC Adv.*, 2016, **6**, 61449–61453.
106 Y. Mai and A. Eisenberg, Self-assembly of block copolymers, *Chem. Soc. Rev.*, 2012, **41**, 5969–5985.
107 Y. Kang, J. J. Walish, T. Gorishnyy and E. L. Thomas, Broad-wavelength-range chemically tunable block-copolymer photonic gels, *Nat. Mater.*, 2007, **6**, 957–960.
108 Y.-B. Baek, S.-H. Choi and D.-M. Shin, Tunable Photonic Band Gap of PS-*b*-P2VP Lamellar Film Using Metal Ions and pH Gradation, *J. Nanosci. Nanotechnol.*, 2015, **15**, 1624–1627.
109 H. S. Lim, J.-H. Lee, J. J. Walish and E. L. Thomas, Dynamic Swelling of Tunable Full-Color Block Copolymer Photonic Gels via Counterion Exchange, *ACS Nano*, 2012, **6**, 8933–8939.
110 Y. Ahn, E. Kim, J. Hyon, C. Kang and Y. Kang, Photonic Crystals: Photoresponsive Block Copolymer Photonic Gels with Widely Tunable Photosensitivity by Counter-Ions, *Adv. Mater.*, 2012, **24**, OP89.
111 J. J. Walish, Y. Fan, A. Centrone and E. L. Thomas, Controlling Thermochromism in a Photonic Block Copolymer Gel, *Macromol. Rapid Commun.*, 2012, **33**, 1504–1509.
112 E.-L. Lin, W.-L. Hsu and Y.-W. Chiang, Trapping Structural Coloration by a Bioinspired Gyroid Microstructure in Solid State, *ACS Nano*, 2017, **12**, 485–493.
113 C.-S. Wu, *et al.*, Flexible or Robust Amorphous Photonic Crystals from Network-Forming Block Copolymers for Sensing Solvent Vapors, *Anal. Chem.*, 2018, **90**, 4847–4855.

114 M. Poutanen, *et al.*, Block Copolymer Micelles for Photonic Fluids and Crystals, *ACS Nano*, 2018, **12**, 3149–3158.
115 D. E. Fogg and H. M. Foucault, Comprehensive Organometallic Chemistry III, *Transit. Met. Catal. Polym. Synth.*, 2007, 623–652, DOI: 10.1016/b0-08-045047-4/00163-1.
116 Y.-G. Yu, *et al.*, Hydrogen Bonding-Mediated Phase Transition of Polystyrene and Polyhydroxystyrene Bottlebrush Block Copolymers with Polyethylene Glycol, *Macromolecules*, 2019, **52**, 4349–4358.
117 H.-B. Seo, Y.-G. Yu, C.-G. Chae, M.-J. Kim and J.-S. Lee, Synthesis of ultrahigh molecular weight bottlebrush block copolymers of ω-end-norbornyl polystyrene and polymethacrylate macromonomers, *Polymer*, 2019, **177**, 241–249.
118 M.-J. Kim, *et al.*, Norbornenyl Macromonomers: In Situ Synthesis by End-Capping of Living Anionic Polymers Using a Norbornenyl-Functionalized α Phenyl Acrylate and Their Ring-Opening Metathesis Polymerization, *Macromolecules*, 2019, **52**, 103–112.
119 Y.-G. Yu, *et al.*, Precise Synthesis of Bottlebrush Block Copolymers from ω End-Norbornyl Polystyrene and Poly(4-tert-butoxystyrene) via Living Anionic Polymerization and Ring-Opening Metathesis Polymerization, *Macromolecules*, 2018, **51**, 447–455.
120 T. Guo, *et al.*, Structure Memory Photonic Crystals Prepared by Hierarchical Self-Assembly of Semicrystalline Bottlebrush Block Copolymers, *Macromolecules*, 2020, **53**, 3602–3610.
121 B. M. Boyle, T. A. French, R. M. Pearson, B. G. McCarthy and G. M. Miyake, Structural Color for Additive Manufacturing: 3D-Printed Photonic Crystals from Block Copolymers, *ACS Nano*, 2017, **11**, 3052–3058.
122 Cypris offers structural coloration with help from the EPA, BASF & better ventures. Focus Pigment, 7 (2023).
123 B. Faure, *et al.*, Dispersion and surface functionalization of oxide nanoparticles for transparent photocatalytic and UV-protecting coatings and sunscreens, *Sci. Technol. Adv. Mater.*, 2013, **14**, 023001.
124 L. Landau and B. Levich Dynamics of Curved Fronts, Part II Collect Pap Dragging Liq Mov Plate 141–153 (1988) , DOI: 10.1016/b978-0-08-092523-3.50016-2.
125 M. Faustini, B. Louis, P. A. Albouy, M. Kuemmel and D. Grosso, Preparation of Sol−Gel Films by Dip-Coating in Extreme Conditions, *J. Phys. Chem. C*, 2010, **114**, 7637–7645.
126 M. Pichumani, P. Bagheri, K. M. Poduska, W. González-Viñas and A. Yethiraj, Dynamics, crystallization and structures in colloid spin coating, *Soft Matter*, 2013, **9**, 3220.
127 E. Guzmán, R. G. Rubio and F. Ortega, A closer physicochemical look to the Layer-by-Layer electrostatic self-assembly of polyelectrolyte multilayers, *Adv. Colloid Interface Sci.*, 2020, **282**, 102197.
128 W. Chen and T. J. McCarthy, Layer-by-Layer Deposition: A Tool for Polymer Surface Modification, *Macromolecules*, 1997, **30**, 78–86.
129 P. Kurt, D. Banerjee, R. E. Cohen and M. F. Rubner, Structural color via layer-by-layer deposition: layered nanoparticle arrays with near-UV and visible reflectivity bands, *J. Mater. Chem.*, 2009, **19**, 8920–8927.
130 X. Yu, W. Ma and S. Zhang, Hydrophobic polymer-incorporated hybrid 1D photonic crystals with brilliant structural colors via aqueous-based layer-by-layer dip-coating, *Dyes Pigm.*, 2021, **186**, 108961.
131 G. M. Nogueira, D. Banerjee, R. E. Cohen and M. F. Rubner, Spray-Layer-by-Layer Assembly Can More Rapidly Produce Optical-Quality Multistack Heterostructures, *Langmuir*, 2011, **27**, 7860–7867.
132 S. Colodrero, M. Ocaña and H. Míguez, Nanoparticle-Based One-Dimensional Photonic Crystals, *Langmuir*, 2008, **24**, 4430–4434.
133 M. E. Calvo and H. Miguez, Flexible, Adhesive, and Biocompatible Bragg Mirrors Based on Polydimethylsiloxane Infiltrated Nanoparticle Multilayers, *Chem. Mater.*, 2010, **22**, 3909–3915.
134 P. Lova, *et al.*, Engineering the Emission of Broadband 2D Perovskites by Polymer Distributed Bragg Reflectors, *ACS Photonics*, 2018, **5**, 867–874.
135 S. Gazzo, *et al.*, High refractive index hyperbranched polyvinylsulfides for planar one-dimensional all-polymer photonic crystals, *J. Polym. Sci., Part B: Polym. Phys.*, 2016, **54**, 73–80.
136 G. Manfredi, C. Mayrhofer, G. Kothleitner, R. Schennach and D. Comoretto, Cellulose ternary photonic crystal created by solution processing, *Cellulose*, 2016, **23**, 2853–2862.
137 G. Giordano, N. Vilà, E. Aubert, J. Ghanbaja and A. Walcarius, Multi-layered, vertically-aligned and functionalized mesoporous silica films generated by sequential electrochemically assisted self-assembly, *Electrochim. Acta*, 2017, **237**, 227–236.
138 G. Giordano, C. Durante, A. Gennaro and M. Guglielmi, Multilayer Deposition of Silica Sol–Gel Films by Electrochemical Assisted Techniques, *J. Phys. Chem. C*, 2016, **120**, 28820–28824.
139 G. Giordano, *et al.*, SiO2–TiO2 multilayer via electrochemical deposition: characterization of reflection and refractive index, *J. Sol-Gel Sci. Technol.*, 2019, **89**, 196–204.
140 W. Zhang, *et al.*, Highly Efficient Perovskite Solar Cells with Tunable Structural Color, *Nano Lett.*, 2015, **15**, 1698–1702.
141 W. Feng, C. Ji and L. J. Guo, Primary and Secondary Reflective Color Realized by Full-Solution-Processed Multi-Layer Structures, *Adv. Opt. Mater.*, 2023, **11**, 2300456.
142 T. Yasuda, K. Nishikawa and S. Furukawa, Structural colors from TiO2/SiO2 multilayer flakes prepared by sol–gel process, *Dyes Pigm.*, 2012, **92**, 1122–1125.
143 W.-J. Feng, Y. Cheng and L. J. Guo, Temporal Coupled Mode Analysis of Chromaticity in Trilayer Subtractive Structural Colors, *ACS Photonics*, 2023, **10**, 2784–2792.
144 G. Pfaff and J. Weitzel, *Color. Plast.*, 2003, 226–241, DOI: 10.1002/0471721581.ch15.
145 F. J. Maile, G. Pfaff and P. Reynders, Effect pigments—past, present and future, *Prog Org Coat*, 2005, **54**, 150–163.

146 F. Keller, M. S. Hunter and D. L. Robinson, Structural Features of Oxide Coatings on Aluminum, *J. Electrochem. Soc.*, 1953, **100**, 411–419.
147 Y. Liu, Y. Chang, Z. Ling, X. Hu and Y. Li, Structural coloring of aluminum, *Electrochem. Commun.*, 2011, **13**, 1336–1339.
148 T. Kikuchi, O. Nishinaga, S. Natsui and R. O. Suzuki, Fabrication of Self-Ordered Porous Alumina via Etidronic Acid Anodizing and Structural Color Generation from Submicrometer-Scale Dimple Array, *Electrochim. Acta*, 2015, **156**, 235–243.
149 O. Yilmaz, M. F. Ebeoglugil, R. Dalmis and T. Dikici, Effect of anodizing time on the structural color and photocatalytic properties of the TiO2 films formed by electrochemical method, *Mater. Sci. Semicond. Process.*, 2023, **167**, 107768.
150 H. N. Umh, S. Yu, Y. H. Kim, S. Y. Lee and J. Yi, Tuning the Structural Color of a 2D Photonic Crystal Using a Bowl-like Nanostructure, *ACS Appl. Mater. Interfaces*, 2016, **8**, 15802–15808.
151 K. Katagiri, *et al.*, Structural color coating films composed of an amorphous array of colloidal particles via electrophoretic deposition, *NPG Asia Mater.*, 2017, **9**, e355–e355.
152 N. Zhou, A. Zhang, L. Shi and K.-Q. Zhang, Fabrication of Structurally-Colored Fibers with Axial Core–Shell Structure via Electrophoretic Deposition and Their Optical Properties, *ACS Macro Lett.*, 2013, **2**, 116–120.
153 C. Ji, S. Acharya, K. Yamada, S. Maldonado and L. J. Guo, Electrodeposition of Large Area, Angle-Insensitive Multilayered Structural Colors, *ACS Appl. Mater. Interfaces*, 2019, **11**, 29065–29071.
154 N. G. Bastus, F. Merkoçi, J. Piella and V. Puntes, Synthesis of Highly Monodisperse Citrate-Stabilized Silver Nanoparticles of up to 200 nm: Kinetic Control and Catalytic Properties, *Chem Mater.*, 2014, **26**, 2836–2846.
155 P. Zhao, N. Li and D. Astruc, State of the art in gold nanoparticle synthesis, *Coord. Chem. Rev.*, 2013, **257**, 638–665.
156 E. S. Kooij, E. A. M. Brouwer, H. Wormeester and B. Poelsema, Ionic Strength Mediated Self-Organization of Gold Nanocrystals: An AFM Study, *Langmuir*, 2002, **18**, 7677–7682.
157 L. Scarabelli, A. Sánchez-Iglesias, J. Pérez-Juste and L. M. Liz-Marzán, A ''Tips and Tricks'' Practical Guide to the Synthesis of Gold Nanorods, *J. Phys. Chem. Lett.*, 2015, **6**, 4270.
158 C. J. Murphy, *et al.*, Gold nanorod crystal growth: From seed-mediated synthesis to nanoscale sculpting, *Curr. Opin. Colloid Interface Sci.*, 2011, **16**, 128–134.
159 X. Ye, *et al.*, Seeded Growth of Monodisperse Gold Nanorods Using Bromide-Free Surfactant Mixtures, *Nano Lett.*, 2013, **13**, 2163–2171.
160 J. Pérez-Juste, I. Pastoriza-Santos, L. M. Liz-Marzán and P. Mulvaney, Gold nanorods: Synthesis, characterization and applications, *Coord. Chem. Rev.*, 2005, **249**, 1870–1901.
161 S. Chen, Z. Fan and D. L. Carroll, Silver Nanodisks: Synthesis, Characterization, and Self-Assembly, *J. Phys. Chem. B*, 2002, **106**, 10777–10781.
162 S. Zhou, *et al.*, Facile Synthesis of Silver Nanocubes with Sharp Corners and Edges in an Aqueous Solution, *ACS Nano*, 2016, **10**, 9861–9870.
163 P. Mao, *et al.*, Manipulating disordered plasmonic systems by external cavity with transition from broadband absorption to reconfigurable reflection, *Nat. Commun.*, 2020, **11**, 1538.
164 P. Mao, *et al.*, Disorder-Induced Material-Insensitive Optical Response in Plasmonic Nanostructures: Vibrant Structural Colors from Noble Metals, *Adv. Mater.*, 2021, **33**, 2007623.
165 J. Kim, H. Oh, M. Seo and M. Lee, Generation of Reflection Colors from Metal–Insulator–Metal Cavity Structure Enabled by Thickness-Dependent Refractive Indices of Metal Thin Film, *ACS Photonics*, 2019, **6**, 2342–2349.
166 Y. H. Kim, *et al.*, Reflection color tuning of a metal–insulator–metal cavity structure using arc plasma deposition of gold nanoparticles, *Appl. Surf. Sci.*, 2021, **562**, 150140.
167 M. A. Rahman, S. M. K. Vivek, S. H. Kim and J. Y. Byun, Polarizonic-interference colouration of stainless steel surfaces by Au-Al2O3 nanocomposite thin film coating, *Appl. Surf. Sci.*, 2020, **505**, 144428.
168 M. Abdelaziz, S. Homaeigohar, M. K. Hedayati, M. A. Assad and M. Elbahri, Solar Aluminum Kitchen Foils with Omnidirectional Vivid Polarizonic Colors, *Adv. Opt. Mater.*, 2019, **7**, 1900737.
169 M. A. Assad, S. Homaeigohar and M. Elbahri, Reflective Coloration from Structural Plasmonic to Disordered Polarizonic, *Adv. Photonics Res.*, 2021, 2100009, DOI: **10.1002/adpr.202100009**.
170 D. Franklin, *et al.*, Self-assembled plasmonics for angle-independent structural color displays with actively addressed black states, *Proc. Natl. Acad. Sci. U. S. A.*, 2020, **117**, 13350–13358.
171 P. Cencillo-Abad, D. Franklin, P. Mastranzo-Ortega, J. Sanchez-Mondragon and D. Chanda, Ultralight plasmonic structural color paint, *Sci. Adv.*, 2023, **9**, eadf7207.
172 S.-J. Kim, H.-K. Choi, H. Lee and S.-H. Hong, Solution-Processable Nanocrystal-Based Broadband Fabry–Perot Absorber for Reflective Vivid Color Generation, *ACS Appl. Mater. Interfaces*, 2019, **11**, 7280–7287.
173 C. Gao, *et al.*, Adsorption of Silver Nanoparticles on Modified Surfaces, *Key Eng. Mater.*, 2015, **645–646**, 75–79.
174 X. Rao, *et al.*, High density gold nanoparticles immobilized on surface via plasma deposited APTES film for decomposing organic compounds in microchannels, *Appl. Surf. Sci.*, 2018, **439**, 272–281.
175 K. R. Brown and M. J. Natan, Hydroxylamine Seeding of Colloidal Au Nanoparticles in Solution and on Surfaces, *Langmuir*, 1998, **14**, 726–728.
176 K. R. Brown, L. A. Lyon, A. P. Fox, B. D. Reiss and M. J. Natan, Hydroxylamine Seeding of Colloidal Au Nanoparticles. 3. Controlled Formation of Conductive Au Films, *Chem. Mater.*, 2000, **12**, 314–323.
177 S. M. Tabakman, Z. Chen, H. S. Casalongue, H. Wang and H. Dai, A New Approach to Solution-Phase Gold Seeding for SERS Substrates, *Small*, 2011, **7**, 499–505.

178 K. R. Brown, D. G. Walter and M. J. Natan, Seeding of Colloidal Au Nanoparticle Solutions. 2. Improved Control of Particle Size and Shape, *Chem. Mater.*, 2000, **12**, 306–313.
179 H. Hulst Christoffel, Light Scattering by Small Particles. (Courier Corporation, 1981).
180 Y. Wu, J. Ren, S. Zhang and S. Wu, Nanosphere-Aggregation-Induced Reflection and Its Application in Large-Area and High-Precision Panchromatic Inkjet Printing, *ACS Appl. Mater. Interfaces*, 2020, **12**, 10867–10874.
181 L. Bai, *et al.*, Large-Scale Noniridescent Structural Color Printing Enabled by Infiltration-Driven Nonequilibrium Colloidal Assembly, *Adv. Mater.*, 2018, **30**, 1705667.
182 J. Ren, *et al.*, Mie resonant structural colors based on ZnO spheres and their application in multi-color Pattern: Especially realization of red color, *Chem. Eng. J.*, 2023, **474**, 145530.
183 J. Ren, Y. Wu, Y. Han, S. Zhang and S. Wu, Noniridescent and Robust Structural-Colored Coating for Automotives Based on the Mie Scattering of ZnO Spheres, *Ind. Eng. Chem. Res.*, 2022, **61**, 18772–18779.
184 Y. Wu, *et al.*, Polarization-Dependent Structural Colors in ZnS Nanosphere-Based Photonic Crystals for Anticounterfeiting Applications, *ACS Appl. Nano Mater.*, 2022, **5**, 423–429.
185 J. Zhou, *et al.*, Visualizing Mie Resonances in Low-Index Dielectric Nanoparticles, *Phys. Rev. Lett.*, 2018, **120**, 253902.
186 Y. Wang, L. Sun, G. Chen, H. Chen and Y. Zhao, Structural Color Ionic Hydrogel Patches for Wound Management, *ACS Nano*, 2023, **17**, 1437–1447.
187 Z. Zhang, *et al.*, Bioinspired Bilayer Structural Color Hydrogel Actuator with Multienvironment Responsiveness and Survivability, *Small Methods*, 2019, **3**, 1900519.
188 A. E. Goodling, S. Nagelberg, M. Kolle and L. D. Zarzar, Tunable and Responsive Structural Color from Polymeric Microstructured Surfaces Enabled by Interference of Totally Internally Reflected Light, *ACS Mater. Lett.*, 2020, **2**, 754–763.
189 S.-U. Kim, *et al.*, Broadband and pixelated camouflage in inflating chiral nematic liquid crystalline elastomers, *Nat. Mater.*, 2022, **21**, 41–46.
190 K. Ku, *et al.*, Effect of Crosslinkers on Optical and Mechanical Behavior of Chiral Nematic Liquid Crystal Elastomers, *Molecules*, 2021, **26**, 6193.
191 K. Ku, *et al.*, Environmentally Stable Chiral-Nematic Liquid-Crystal Elastomers with Mechano-Optical Properties, *Appl. Sci.*, 2021, **11**, 5037.
192 C. Liu, *et al.*, Dynamic Color Display with Viewing-Angle Tolerance Based on the Responsive Asymmetric Fabry–Perot Cavity, *ACS Appl. Mater. Interfaces*, 2022, **14**, 7200–7207.
193 K. Higashiguchi, N. Morita and K. Matsuda, Structural Colored Balloon Composed of Temperature-Responsive Polymers Showing LCST Behavior, *Langmuir*, 2018, **34**, 12853–12860.
194 Y. Wang, Q. Zhao and X. Du, Inkless multi-color writing and copying of laser-programmable photonic crystals, *Mater. Horiz.*, 2020, **7**, 1341–1347.
195 C. Huang, Y. Shang, J. Hua, Y. Yin and X. Du, Self-Destructive Structural Color Liquids for Time–Temperature Indicating, *ACS Nano*, 2023, **17**, 10269–10279.
196 C. Sun, *et al.*, Bioinspired Hydrophobic Cellulose Nanocrystal Composite Films as Organic-Solvent-Responsive Structural-Color Rewritable Papers, *ACS Appl. Mater. Interfaces*, 2020, **12**, 26455–26463.
197 C. Ji, J. Zeng, S. Qin, M. Chen and L. Wu, Angle-independent responsive organogel retroreflective structural color film for colorimetric sensing of humidity and organic vapors, *Chin. Chem. Lett.*, 2021, **32**, 3584–3590.
198 S. D. Rezaei, *et al.*, Tunable, Cost-Effective, and Scalable Structural Colors for Sensing and Consumer Products, *Adv. Opt. Mater.*, 2019, **7**, 1900735.
199 F. Xue, *et al.*, Two-dimensional inverse opal hydrogel for pH sensing, *Analyst*, 2014, **139**, 6192–6196.
200 H. Yang, *et al.*, Color-spectrum-broadened ductile cellulose films for vapor-pH-responsive colorimetric sensors, *J. Ind. Eng. Chem.*, 2019, **80**, 590–596.
201 J. Liao, *et al.*, Multiresponsive Elastic Colloidal Crystals for Reversible Structural Color Patterns, *Adv. Funct. Mater.*, 2019, **29**, 1902954.
202 K. Higashiguchi, J. Imai and K. Matsuda, Structural Colored Balloons Responsive to pH Change, *Langmuir*, 2016, **32**, 4945–4951.
203 Y. Xia, *et al.*, Near-Infrared Light Induced Dynamic Structural Color Change of Amorphous Photonic Hydrogel, *ACS Appl. Polym. Mater.*, 2021, **3**, 757–764.
204 M. Xiong, *et al.*, Power-Free and Self-Cleaning Solar Light Detector Based on the Temperature-Sensitive Structural Color and Photothermal Effect, *ACS Appl. Mater. Interfaces*, 2021, **13**, 33566–33573.
205 A. Belmonte, *et al.*, Dual Light and Temperature Responsive Micrometer-Sized Structural Color Actuators, *Small*, 2020, **16**, e1905219.
206 W. Zhao, *et al.*, Visual multi-triggered sensor based on inverse opal hydrogel, *Colloids Surf., A*, 2018, **554**, 93–99.
207 C. Liu, Z. Fan, Y. Tan, F. Fan and H. Xu, Tunable Structural Color Patterns Based on the Visible-Light-Responsive Dynamic Diselenide Metathesis, *Adv. Mater.*, 2020, **32**, 1907569.
208 O. N. Oliveira, M. Raposo and A. Dhanabalan, *Handbook of Surfaces and Interfaces of Materials*, 1–63, (2001), DOI: **10.1016/b978-012513910-6/50047-5**.
209 J. Park, S. Yoon, N. Heo and W. Lee, Electrochromic inverse opal photonic gel containing charged hydrogel in aqueous media for full color reflective display, *J. Ind. Eng. Chem.*, 2020, **88**, 117–126.
210 A. A. F. Froyen, *et al.*, Ink-Deposited Transparent Electrochromic Structural Colored Foils, *ACS Appl. Mater. Interfaces*, 2022, **14**, 39375–39383.
211 S. Zhang, *et al.*, Reflective Structural Color Tunability of Inorganic Electrochromic Devices by Interferometric Modulation, *Int. J. Nanosci.*, 2021, **20**, 2150054.
212 H.-Y. Qu, *et al.*, Multicolored absorbing nickel oxide films based on anodic electrochromism and structural coloration, *J. Appl. Phys.*, 2021, **129**, 123105.

213 X. Ran, J. Ren, S. Zhang, Y. Wu and S. Wu, Multicolor Electrochromic Display and Patterned Device Based on Hollow-SiO2-Supported WO3 Photonic Crystals, *ACS Appl. Mater. Interfaces*, 2023, **15**, 41763–41771.

214 M. Seo, *et al.*, Printing of Highly Vivid Structural Colors on Metal Substrates with a Metal-Dielectric Double Layer, *Adv. Opt. Mater.*, 2019, **7**, 1900196.

215 M. A. Rahman, D. K. Kim, J.-K. Lee and J. Y. Byun, To realize a variety of structural color adjustments via lossy-dielectric-based Fabry–Perot cavity structure, *Nanophotonics*, 2022, **11**, 4855–4868.

216 S. Rossi and M. P. Jonsson, Highly reflective optical nanocavities for structural coloration by combining broadband absorber and FabryProt effects, *J. Optom.*, 2021, **23**, 015001.

217 M. A. Kats, R. Blanchard, P. Genevet and F. Capasso, Nanometre optical coatings based on strong interference effects in highly absorbing media, *Nat. Mater.*, 2013, **12**, 20–24.

218 S. Ayas, *et al.*, Colorimetric detection of ultrathin dielectrics on strong interference coatings, *Opt. Lett.*, 2018, **43**, 1379–1382.

219 O. Hemmatyar, S. Abdollahramezani, Y. Kiarashinejad, M. Zandehshahvar and A. Adibi, Full color generation with Fano-type resonant HfO2 nanopillars designed by a deep-learning approach, *Nanoscale*, 2019, **11**, 21266–21274.

220 A. S. Rana, M. Zubair, M. S. Anwar, M. Saleem and M. Q. Mehmood, Engineering the absorption spectra of thin film multilayer absorbers for enhanced color purity in CMY color filters, *Opt. Mater. Express*, 2020, **10**, 268.

221 D. Kim, *et al.*, Manipulation of resonance orders and absorbing materials for structural colors in transmission with improved color purity, *Opt. Express*, 2022, **30**, 11740.

222 C. Yang, *et al.*, Tunable, omnidirectional structural color on reflection based on metal-SiOx-metal structure, *Appl. Phys. Lett.*, 2016, **109**, 241104.

223 C.-S. Park, V. R. Shrestha, S.-S. Lee, E.-S. Kim and D.-Y. Choi, Omnidirectional color filters capitalizing on a nano-resonator of Ag-TiO2-Ag integrated with a phase compensating dielectric overlay, *Sci. Rep.*, 2015, **5**, 8467.

224 K. Lee, S. Seo and L. J. Guo, High-Color-Purity Subtractive Color Filters with a Wide Viewing Angle Based on Plasmonic Perfect Absorbers, *Adv. Opt. Mater.*, 2015, **3**, 347–352.

225 Z. Yang, C. Ji, D. Liu and L. J. Guo, Enhancing the Purity of Reflective Structural Colors with Ultrathin Bilayer Media as Effective Ideal Absorbers, *Adv. Opt. Mater.*, 2019, **7**, 1900739.

226 H. Pan, *et al.*, Wide gamut, angle-insensitive structural colors based on deep-subwavelength bilayer media, *Nanophotonics*, 2020, **9**, 3385–3392.

227 C. J. Huang, K. C. Liao and Y. K. Su, Structure Property of Titanium Dioxide Thin Films in Sintered Temperature by the Sol-Gel Method, *Key Eng. Mater.*, 2008, **368–372**, 1465–1467.

228 V. Lucarini, K.-E. Peiponen, J. J. Saarinen and E. M. Vartiainen, Kramers-Kronig Relations in Optical Materials Research, *Springer Ser. Opt. Sci.*, 2005, **110**, 1, DOI: **10.1007/b138913**.

229 E. Rio and F. Boulogne, Withdrawing a solid from a bath: How much liquid is coated?, *Adv. Colloid Interface Sci.*, 2017, **247**, 100–114.

230 Q. Yang and L. R. Zhao, Characterization of nano-layered multilayer coatings using modified Bragg law, *Mater. Charact.*, 2008, **59**, 1285–1291.

231 M. Born *et al.*, *Principles of Optics*, (1999), DOI: **10.1017/cbo9781139644181**.

232 B. T. Mekonnen, *et al.*, Preparation of aerogel and its application progress in coatings: a mini overview, *J. Leather Sci. Eng.*, 2021, **3**, 25.

233 H.-S. Yang, S.-Y. Choi, S.-H. Hyun, H.-H. Park and J.-K. Hong, Ambient-dried low dielectric SiO2 aerogel thin film, *J. Non-Cryst. Solids*, 1997, **221**, 151–156.

234 P. Lin, M. Mah and J. J. Talghader Synthesis and Characterizations of a Very Low Index Silica Aerogel Optical Thin Film, Opt Interf Coatings Conf Oic 2022 WD.5 (2022) , DOI: **10.1364/oic.2022.wd.5**.

235 S. H. Hyun, J. J. Kim and H. H. Park, Synthesis and Characterization of Low-Dielectric Silica Aerogel Films, *J. Am. Ceram. Soc.*, 2000, **83**, 533–540.

236 S. S. Prakash, C. J. Brinker, A. J. Hurd and S. M. Rao, Silica aerogel films prepared at ambient pressure by using surface derivatization to induce reversible drying shrinkage, *Nature*, 1995, **374**, 439–443.

237 C. Liu, *et al.*, Enhanced energy storage in chaotic optical resonators, *Nat. Photonics*, 2013, **7**, 473–478.

238 Y. Y. Yu, S. S. Chang, C. L. Lee and C. C. Wang, Gold Nanorods: Electrochemical Synthesis and Optical Properties, *J. Phys. Chem. B*, 1997, **101**, 6661–6664.

239 Y. Niidome, H. Takahashi, S. Urakawa, K. Nishioka and S. Yamada, Immobilization of Gold Nanorods on the Glass Substrate by the Electrostatic Interactions for Localized Plasmon Sensing, *Chem. Lett.*, 2004, **33**, 454–455.

240 C. Kuttner, *et al.*, Seeded Growth Synthesis of Gold Nanotriangles: Size Control, SAXS Analysis, and SERS Performance, *ACS Appl. Mater. Interfaces*, 2018, **10**, 11152–11163.

241 Y.-H. Chang, W.-H. Hsu, S.-L. Wu and Y.-C. Ding, The synthesis of a gold nanodisk–molecular layer–gold film vertical structure: a molecular layer as the spacer for SERS hot spot investigations, *Mater. Chem. Front.*, 2016, **1**, 922–927.

242 B. Saute and R. Narayanan, Solution-based direct readout surface enhanced Raman spectroscopic (SERS) detection of ultra-low levels of thiram with dogbone shaped gold nanoparticles, *Analyst*, 2010, **136**, 527.

243 Y. Sun and C. An, Shaped gold and silver nanoparticles, *Front. Mater. Sci.*, 2010, **5**, 1–24.